

Part 3

APPLICATIONS

In the two previous parts it was shown how images of objects can be obtained and processed in order to extract useful information about the objects. In this part different applications of image processing and analysis techniques to solve real problems are discussed. The first application shows how image analysis can be used in environmental research on aerosols. A method for the classification of individual aerosol particles into two main groups, fly ash and soil dust, according to their shape is presented. The obtained results allow the unequivocal identification of the particle source, which is especially important when the chemical composition of the particles is nearly the same. The second application is also related to environmental research. It is shown how the differentiation between individual algae cells and their agglomerates can be done using information obtained from the analysis of their shape. The results show the ability of the developed method to perform this type of classification. The third example is related to the material research. A method for the classification of individual tabular grain silver halide microcrystals into three main groups, namely, hexagonal, regular triangular and truncated triangular microcrystals, according to their shape is presented. Often microcrystals are partially overlapping as seen in the SEM images and they form irregularly shaped ensembles. A method to reconstruct the microcrystals from such ensembles is also presented. The methods can be used for fast analysis of the shape of microcrystals which is especially important for the development of photographic materials. The last application is related to study of many-particle systems. The unique physical and chemical properties of such systems make them of great fundamental interest. Image analysis in combination with zero-loss electron spectroscopic imaging is applied to study many-particle systems and percolation networks.

3.1. Classification of individual fly ash and soil dust aerosol particles

A method for the classification of individual aerosol particles into one of two main groups, namely, fly ash and soil dust, is discussed. It is based on the calculation of the fractal dimension of the images of the particles obtained with the computer-controlled scanning electron microscope. The risk of an improper determination of the fractal dimension is pointed out. It is shown that spherically shaped particles do not possess fractality. The rarely met fly ash particles with very irregular shape possess two types of the fractal dimensions, namely, textural and structural. On the other hand, it is found that the soil dust particles have only a textural fractal dimension. The obtained results allow the unequivocal identification of the particle source, which is especially important when the chemical composition of the particles is nearly the same.

3.1.1. Introduction

Analysis of individual aerosol particles can yield very important environmental information, the relevance of which cannot be overestimated. However, the identification and apportionment of the sources of the particles is often complicated because particles, originating from different sources, can have similar compositions. The most widespread example is fly ash (usually originating from combustion) and soil dust particles (usually clay minerals) which have nearly the same compositions (Fig. 3.1.1). The only parameter, which allows to differentiate between them, is the shape. Therefore, the characterization of the shape of aerosol particles is very genuine. The problem is, however, in revealing and representing the shape.

At least, four different methods of aerosol particle shape representation are possible [3.1.1]. The first and the oldest one is based on different shape factors. The main disadvantage is that shape factors are integral characteristics and, as such, may not be sensitive enough to the details of the particle shape. The other three methods are fractal and Fourier analyses and chain coding. Chain coding has been used for shape description while Fourier analysis is a well-established method of shape characterization. The fractal approach to shape characterization certainly is more exotic although there are numerous works [3.1.2, 3.1.3], which deal with the determination of fractal dimension, [3.1.4-3.1.6], where fractal approach is applied to the description of the shape of different particles. In the present study the applicability of fractals for morphological description of the shapes of individual aerosol particles studied with computer-controlled scanning electron microscopy in combination

with energy-dispersive X-ray microanalysis (CC SEM-EDX) is examined.

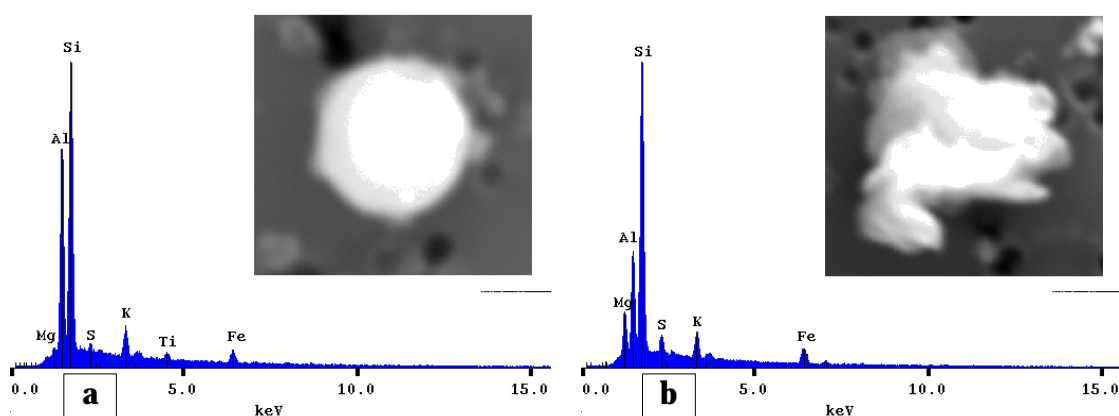


Fig. 3.1.1. a) spherically shaped fly ash and b) irregularly shaped soil dust aerosol particles have similar chemical compositions.

3.1.2. Types of shapes of aerosol particles

Aerosol particles are characterized by a large variety of sizes and shapes. The shape of the particle is mainly determined by its origin. When dealing with continental aerosols, two main types of aerosol particles, viz. fly ash and soil dust, can be observed. Fly ash originates from various kinds of combustion processes (power plants, metallurgical plants, cars and other urban sources, etc.), whereas soil dust originates from soil or earth crust dispersion. As a consequence, soil dust particles have a rather pronounced, sometimes very irregular, shape. According to light microscopy studies [3.1.7], fly ash particles can be classified into eleven shape classes, viz.: 1) amorphous, nonopaque; 2) amorphous, opaque; 3) amorphous, mixed opaque and nonopaque; 4) rounded, vesicular, nonopaque; 5) rounded, vesicular, mixed opaque and nonopaque; 6) angular, lacy, opaque; 7) nonopaque, cenosphere; 8) nonopaque, plerosphere; 9) nonopaque, solid sphere; 10) opaque sphere; 11) nonopaque sphere with crystals. SEM investigations [3.1.8] allow to recognize seven categories of ash particles, namely: 1) unfused detrital minerals (principally quartz); 2) irregular-spongy particles derived from partly-fused clay minerals; 3) vesicular colourless glass (in the form of irregular particles and cenospheres), derived from viscous melts; 4) solid glass (mostly in the form of spherical particles), derived from fluid melts; 5) dendritic iron oxide particles (mostly spherical); 6) crystalline iron oxide particles (mostly spherical); and 7) unburnt char particles. However, in spite of a such variety of shapes, spherical particles are the most abundant. Depending on the size distribution their relative abundance reaches sometimes 86% [3.1.7].

The composition of the fly ash particles is not so variable as their shape. Among the two

main classes there are particles rich in silicon and aluminum oxides (main fraction), and those, rich in iron oxide [3.1.8]. As regards the soil dust particles, aluminosilicates constitute their main fraction.

Summarizing, it can be stated that soil dust particles normally have pronounced, irregular shapes, whereas the majority of the fly ash particles have spherical shapes, and limited number of fly ash particles show a very irregular shape. The composition of most of the fly ash and soil dust particles is very similar. In order to study the possibilities of the fractal characterization of the shape, the following three different types of particles were examined: 1) soil dust; 2) fly ash of spherical shape; and 3) fly ash with irregular shape.

3.1.3. Fractal description of particle shapes: a brief overview

From the specific point of view of shape characterization of microscopic particles the main aim of the fractal approach is to find a 'measure' to distinguish between curves with different, often very complicated, contours. The main idea is to describe the complexity of the curve through a new parameter, the fractal dimension, so as to fill in the gap between one- and two-dimensional objects (for objects on a plane). The more complex the contour of the curve, the more it covers the plane in a dense manner and the more its fractal dimension will be close to 2.

The fractal concept is not strictly defined. In spite of this there is a consensus that fractal objects (among other important features) normally possess a too irregular structure to be described by traditional geometrical or topological approaches. The main characteristic of fractals is their fractal dimension which can be introduced in different ways. As applied to particle shape characterization it can be established in the following way. As a consequence of the very irregular structure, the perimeter of the contour depends on the length of the 'stride' or 'yardstick' with which the measurements were performed. A smaller yardstick can take into account details of the (complicated) shape which are 'invisible' with larger strides. Therefore, the smaller the 'step' L , the larger the perimeter P measured with it. This dependence can be mathematically expressed as $P \propto L^\alpha$ where α is the slope of the line observed in the 'perimeter vs. yardstick' log-log plot. Just this slope is directly connected to the fractal dimension D as $D = 1 - \alpha$. From the above given explanation it is obvious that α is negative, so $D > 1$. The method which is based on this idea, is called 'hand and dividers' method. Its mathematical basic is discussed in Part 2, here some practical problems of its application are shown.

An important remark regarding the form of these log-log plots in the framework of the

present problem needs to be made. As it was supposed [3.1.9], 'true' fractals should have a single straight line over the whole range of the 'yardsticks' used. Within the framework of the present study 'true' fractals can be referred to as objects which have a shape that possesses 'self-similarity'. 'Self-similarity' means that the main 'construction elements' of the contour of the object can be seen for the whole range of the strides. In other words, the higher the magnification with which the object is observed, the more details can be seen, but the shape of these details is the same for all magnifications. However, in practice, self-similarity is seldom observed [3.1.6, 3.1.10] and usually two straight lines are seen on the log-log plots. One of them is commonly considered as reflecting the 'textural' fractal dimension, whereas the other one describes the 'structural' one [3.1.6]. They can be referred to as the microscopic and macroscopic descriptions of the contour shape.

In the majority of references (e.g. [3.1.6]) the fractal dimension (especially the textural dimension) is determined using only 5, 4, 3 and even 2(!) points on the log-log plot. Often the difference between the two fractal dimensions (between the slopes of the two straight lines) looks insignificant, but no statistical information is provided. Moreover, the so-called 'textural' fractals can appear only as a result of the discrete nature of the computer images. Indeed, a circle has definitely no fractality. Fig. 3.1.2 presents the results of fractal analysis of the digital image of a circle. It is seen that the first 3 points (corresponding to the first three 'yardsticks' used) exhibit a kind of 'statistically significant dependence'. A false 'textural' fractal dimension is observed. False fractals are called 'fractal rabbits' following the example of Prof. D. Avnir [3.1.6]. This artificial example of 'fractal rabbit' demonstrates that one should be extremely careful dealing with fractals.

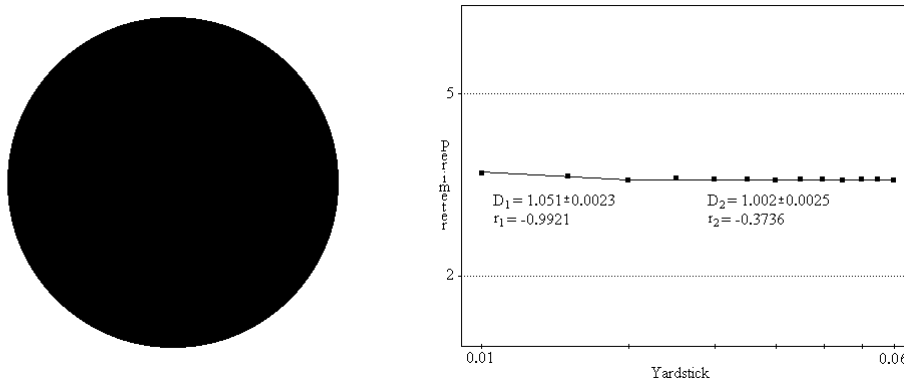


Fig. 3.1.2. Fractal analysis of the shape of an image of a circle. Here and in the subsequent Figs 3.1.3, 3.1.4 and 3.1.5 the following designations are used: r - the coefficient of correlation for the given regression straight line, D - fractal dimension. The yardstick is measured in fractions of Feret's diameter.

3.1.4. Experimental

The particles, which were used in the present study, were collected in two different sampling campaigns. First, particles collected in Southern Siberia, Russia, during the winter of 1992 were used. From February 5th to March 4th 1992, aerosol samples were collected 3 times a day in Karasuk, a relatively small and remote town some 400 km west of Novosibirsk. The sampling equipment was placed some 8 km west of the town on the shore of a small lake. The sampler was positioned approximately 2 m above the ground. The particles were collected using 47 mm diameter, 0.4 μm pore size Nuclepore polycarbonate membrane filters (aerosol grade). These filters were placed in plexiglass filter holders with a hat-type cover to protect them from rain. The vacuum pump equipped with a flow meter, was operated at a flow rate of approximately 50 l/min. In this case most of the particles were spherically shaped fly ash particles.

Other aerosol particles were collected during a forest fire in the delta of the river Podkamennaya Tunguska in Russia on July 6th, 1993. The sampling equipment was lifted above the fire with the help of a helicopter. A small sampler for material dispersed by the fire was loaded with 0.4 μm pore-sized Nuclepore filters. Aerosols were sampled during numerous flights through the smoke column. In this way samples with irregularly shaped fly ash particles were acquired.

The measurements were performed on a JEOL JSM-6300 electron microscope using an electron energy of 20 keV and a beam current of ca. 1 nA and typical magnification ca 5000x. This CC SEM-EDX is equipped with a Si(Li) detector that can work in windowless mode (PGT-IMIX). Images of some one hundred aerosol particles were acquired.

Median filtering was used to decrease the noise and increase the signal/background ration of the images. Then the filtered 8 bit gray level images were converted into binary ones by a manual thresholding. The bottom-to-top left-to-right procedure which is described in Part 1, was applied in order to locate the particle in the binary image. Contours of the images of aerosol particles were extracted from their binary images by the crack following technique (Part 1) and stored as a list of coordinates. Fractal dimension is calculated from the contour's coordinates using the following method. For a given yardstick size L , the perimeter of the object is determined as follows. Starting at some arbitrary contour point (x_s, y_s) the next point on the contour (x_n, y_n) in clockwise direction is located which has a distance d_j as close as possible to L . This point is then used to locate the next point on the contour that satisfies this condition. The process is repeated until the initial starting point is reached. The perimeter is the sum of all distances d_j including the distance between the last located point and the starting point. These calculations are performed for different yardstick sizes. Next, the perimeter is plotted vs. the yardstick size on the log-log plot. Regression analysis is used

to obtain the slope of the line observed on the log-log plot. Image preprocessing and fractal dimension calculation were performed with software developed as part of this thesis.

It is interesting to note that the procedure is practically independent on the choice (of course, in reasonable limits) of the threshold when converting a 256 gray-scale image into a binary one. This fact is illustrated in Table 3.1.1 where fractal dimensions and their root mean square errors for 16 different thresholds of the image of a soil dust aerosol particle which is presented in Fig. 3.1.5, are given.

Threshold	Feret's diameter	Coefficient of correlation	Fractal dimension	Root mean square error
100	285.5	-0.96	1.039	±0.0071
105	284.0	-0.97	1.040	±0.0062
110	282.1	-0.94	1.037	±0.0080
115	278.4	-0.97	1.045	±0.0071
120	278.7	-0.89	1.031	±0.0097
125	276.7	-0.91	1.034	±0.0094
130	276.0	-0.94	1.042	±0.0093
135	174.3	-0.96	1.047	±0.0074
140	273.2	-0.95	1.044	±0.0081
145	271.4	-0.91	1.036	±0.0094
150	267.0	-0.96	1.049	±0.0084
160	267.2	-0.95	1.042	±0.0058
170	264.2	-0.96	1.039	±0.0066
180	256.6	-0.96	1.035	±0.0059
190	249.0	-0.98	1.047	±0.0052
200	244.4	-0.97	1.056	±0.0085

Table 3.1.1. Values of Feret's diameters, coefficients of correlation of linear regression straight lines, fractal dimensions and their root mean square errors for different thresholds of the image of soil dust particle shown in Fig. 3.1.5.

3.1.5. Results and discussion

A typical example of a spherical fly ash particle, its EDX spectrum and the results of the fractal analysis are presented in Fig. 3.1.3. The first three points on the log-log plot demonstrate a type of 'dependence' which can be attributed to the digital nature of the image (fractal rabbit). The coefficient of correlation seems reliable, the fractal dimension differs statistically significantly from unity. The 2nd straight line obviously demonstrates the absence of fractality for this spherically shaped fly ash particle. So, it can be concluded that spherically shaped particles do not possess fractality.

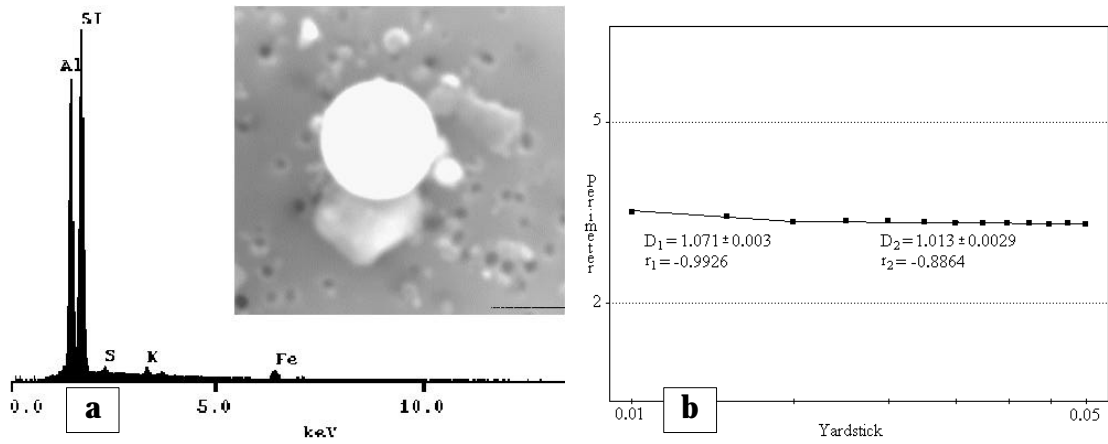


Fig. 3.1.3. a) SEM micrograph, EDX spectrum and b) results of fractal analysis of a spherically shaped fly ash particle.

A picture of a fly ash particle with very irregular shape, its EDX spectrum and the results of fractal analysis are given in Fig. 3.1.4. The differences in the composition as well as the differences in shape compared to the previously studied fly ash particle are explained by the different origin. Consequently, the results of the fractal analysis are also different. Two different dependencies are seen in on the log-log plot, corresponding to two different fractal dimensions. It is interesting to note that no 'fractal rabbits' are observed. The irregularly shaped fly ash particles possess two-mode fractal dimensions with significant statistical difference between the dimensions.

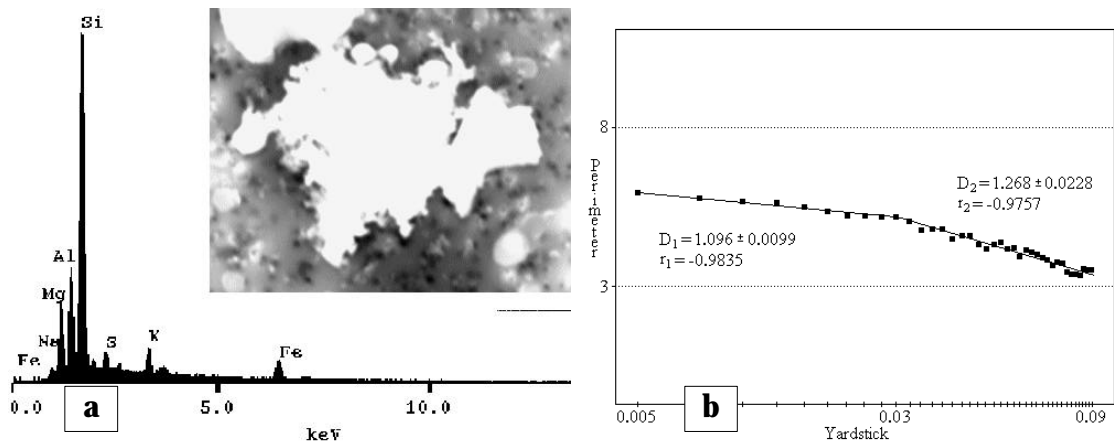


Fig. 3.1.4. a) SEM micrograph, EDX spectrum and b) results of fractal analysis of an irregularly shaped fly ash particle.

A micrograph of a soil dust particle, its EDX spectrum and the results of fractal analysis are shown in Fig. 3.1.5. Comparison of Figs 3.1.3 and 3.1.5 leads to the conclusion that it is impossible to judge about belonging of the particle to the fly ash or soil dust classes solely on the base of the composition. At the same time, fractal analysis reveals interesting things. The first three points (which are not shown in the graph) form a 'fractal rabbit' just as in the case of the spherically shaped fly ash particle. At the same time, textural fractality is evident from the log-log plot. The 'yardsticks' larger than 0.05 of Feret diameter do not possess any kind of dependence, indicating the absence of a structural fractality.

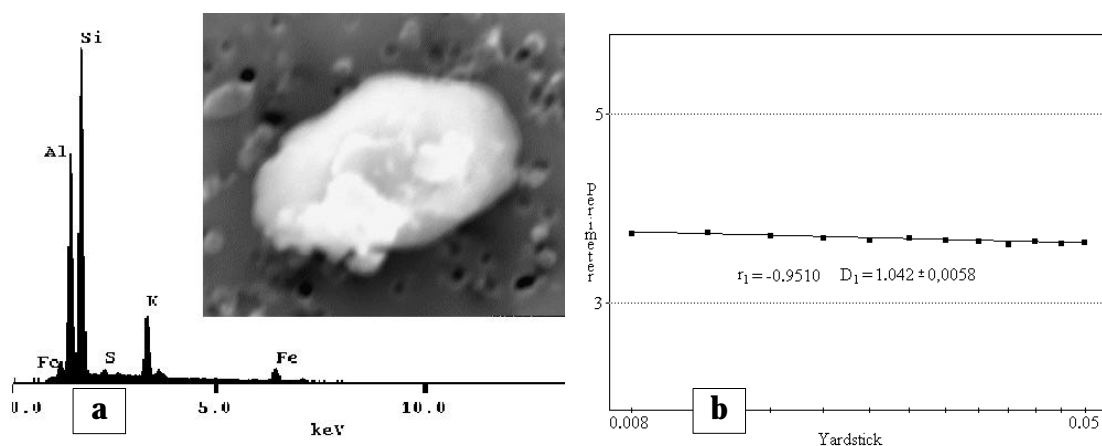


Fig. 3.1.5. a) SEM micrograph, EDX spectrum and b) results of fractal analysis of an irregularly shaped soil dust particle.

Type of aerosol particle	Number of particles studied	Fractal dimension	
		Textural	Structural
spherically shaped fly ash	35	no	no
irregularly shaped fly ash	21	1.09 ± 0.015	1.28 ± 0.020
soil dust	37	1.04 ± 0.013	no

Table 3.1.2. Fractal diameters \pm standard deviations for three different types of individual aerosol particles.

The results of studying these three types of individual aerosol particles are summarized in Table 3.1.2. The values of the fractal dimensions of the particles of the same class vary significantly. However, the phenomena of the absence of fractality for the spherically shaped

fly ash particles, the presence of both textural and structural fractality for the irregularly shaped fly ash particles and of only textural fractality for soil dust particles hold for all the particles studied.

3.1.6. Conclusions

The results of the fractal analysis of the SEM images of the two main types of fly ash particles (spherically shaped and with irregular forms) show that they have a different fractal behavior. Spherically shaped particles have no fractality at all, whereas irregularly shaped particles are characterized by both textural and structural fractal dimensions. Soil dust particles, in turn, can be characterized only by textural fractal dimension. The regularities found can be used for the unequivocal differentiation between soil dust and fly ash particles thus allowing correct particle source apportionment.

3.2. Differentiation between individual algae cells and their agglomerates

A method for the differentiation between individual algae cells and their agglomerates according to their shape is discussed. Ideas on the functional approach to shape analysis, discussed in Part 2, are used. The method is based on the application of complex Fourier descriptors which are obtained from the SEM images of the cells. It is shown how such descriptors can be obtained and used to differentiate between the individual cells and their agglomerates as seen in SEM images. Different classification algorithms, namely, hierarchical cluster analysis and a neural network based classifier, are used to perform a quantitative analysis of a collected population of algae cells and agglomerates and to classify individual objects. The obtained results show the ability of the developed method to perform the identification of the algae cells and their agglomerates according to their shape.

3.2.1. Introduction

SEM images of an individual algae cell and a cell agglomerate are shown in Fig. 3.2.1. During further automated analysis one is only interested in individual cells, creating the need to differentiate automatically between them and their agglomerates.

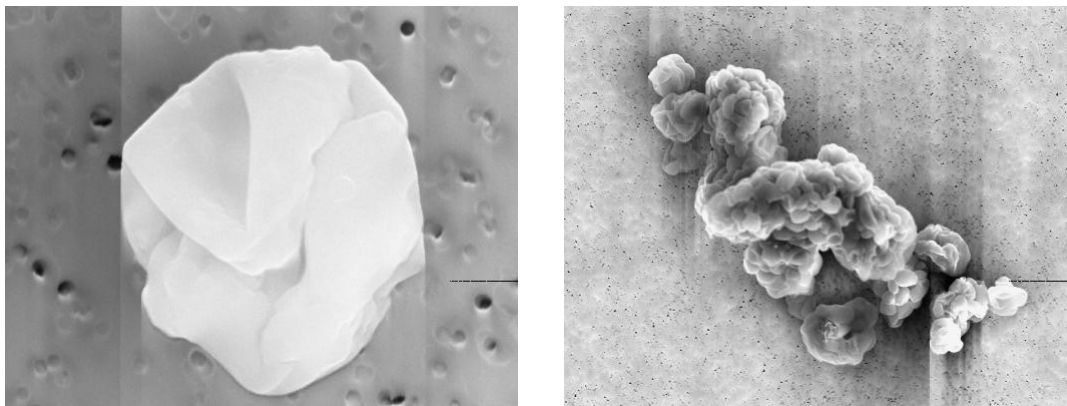


Fig. 3.2.1. SEM images of an individual algae cell and a cell agglomerate.

Algae cells and especially their agglomerates show a large variety of possible shapes. Their description is rather complicated and can be hardly standardized. It was found, for example, that fractal approach, which was previously successfully applied for aerosol particles, is not sensitive enough to differentiate between some individual cells and cell agglomerates. A more

complex technique, based on complex Fourier descriptors, has been developed to perform the differentiation between the cells and their agglomerates.

3.2.2. Complex Fourier shape description

Fourier descriptors calculated from complex Fourier series expansion were successfully used for characterization and classification of various objects having pre-defined shapes (e.g. aircrafts [3.2.1]). The advantage of using this approach for pre-defined shapes is the possibility to use an iterative type of classification algorithms which searches for the optimum match between the unknown shape and each reference shape. For the given problem such algorithms are ineffective because there is no reference shape for both an algae cells and cell agglomerates. So, essential modifications of this method have been done in order to apply it for the classification of algae cells and their agglomerates.

In classical complex Fourier analysis, as described in Part 2, the shape parameters used are the amplitudes of the Fourier spectra. They also can be used in the framework of the present problem, however, additional preprocessing of the contours of the cells and agglomerates should be done in order to represent them in the same way and, therefore, make an interpretation of the obtained results more clear and convenient. It has been done as follows.

1. The contour's center of mass (x_m, y_m) is determined and new contour coordinates are calculated: $(x_{new}(j), y_{new}(j)) = (x(j) - x_m, y(j) - y_m)$. After this translation the contour's center of mass has the coordinates $(0, 0)$.
2. The largest distance d from the center of mass to the contour is calculated and the new contour coordinates are calculated as follows: $(x_{new}(j), y_{new}(j)) = (x(j)/d, y(j)/d)$. In this way the contour's size is normalized.
3. The point (x', y') of a contour for which the distance d to the center of mass is largest is found and the contour is rotated around the center of mass as follows:

$$(x_{new}(j), y_{new}(j)) = \left(\sqrt{x^2(j) + y^2(j)} \cos(\alpha + \beta(j)), \sqrt{x^2(j) + y^2(j)} \sin(\alpha + \beta(j)) \right)$$

where $\beta(j)$ is the angle between the vectors $(x(j), y(j))$ and $(1, 0)$ and α is the angle between the vectors (x', y') and $(1, 0)$. After this rotation the point (x', y') is moved to the position $(1, 0)$ and is used as the starting point of the contour.

4. The number of the complex coefficients needed to reconstruct the contour is equal to the number of the points of the contour. In practice such description is too large for classification purposes. Moreover the descriptor obtained in this way has a different number of the coefficients for different contours so they cannot be compared. To eliminate this problem the contour should be resampled to make the total number of the contour's points

equal for all contours and as small as possible. This resampling was done by a polygonal approximation of the contours using a method based on the intrinsic equation of a curve as described in Part 2. Examples of the original and the resampled contours together with corresponding complex Fourier shape descriptors are shown in Fig. 3.2.2.

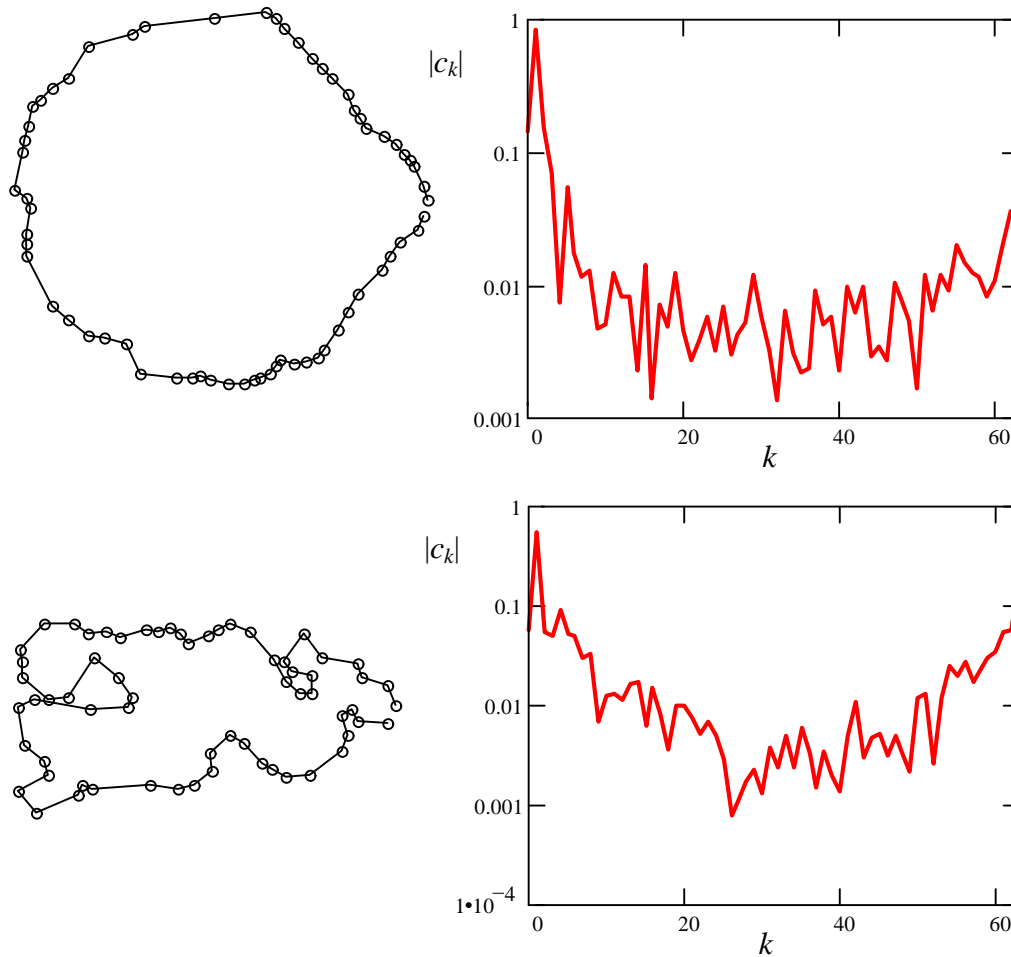


Fig. 3.2.2. Original and resampled contours of an individual algae cell and a cell agglomerate shown in Fig. 3.2.1 and their Fourier shape descriptors.

3.2.3. Classification algorithms

Supervised and unsupervised methods of classification were used to test the applicability of the Fourier shape descriptor, derived as shown above, for the classification of the cells and their agglomerates.

Unsupervised classification was performed using hierarchical cluster analysis [3.2.2] as

implemented in the IDAS software [3.2.3]. The aim of hierarchical clustering is to find groups of objects with similar properties. The objects (algae cells and their agglomerates) in this particular case are represented by their Fourier descriptors and the clustering allows to find objects having similar Fourier descriptors. The results of the hierarchical clustering are represented as a dendrogram.

Supervised classification was performed with a three-layer feedforward neural network trained using the stochastic back propagation training technique [3.2.4] as implemented in NeuFrame software [3.2.5]. For the input layer having 64 neurons a linear transfer function was used, whereas for the hidden layer having 8 neurons and the output layer having 1 neuron sigmoidal transfer functions were used. The neural network is shown in Fig. 3.2.3a. The network was trained on a very limited training set consisting of the shape descriptors of 3 randomly chosen cell agglomerates and 6 randomly chosen individual cells. At the output layer 0 corresponded to an agglomerate and 1 to an individual cell. A random error of 0.01 was added to the training set during the training of the neural network. The training was performed until the error reached its lowest value of 0.05 after 612 complete passes through the set of training data. The error graph of the training cycle is given in Fig. 3.2.3b.

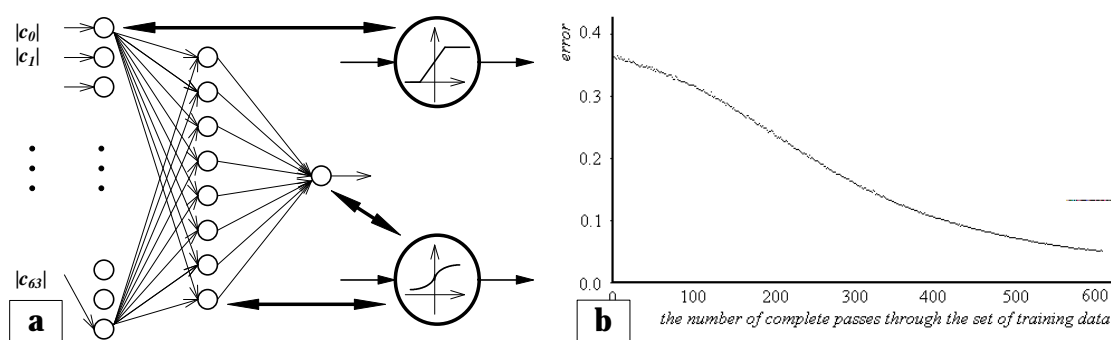


Fig. 3.2.3. a) a schematic representation of the neural network used in the present study; **b)** the error graph of the training cycle of the network.

3.2.4. Experimental

Since the samples were provided as dry powders, they could not be analyzed directly by SEM but had to be transferred and spread onto a suitable substrate for single particle analysis. Well separated particles were produced by the liquid suspension technique [3.2.6] as follows. A small portion of the powder is dispersed in an inert liquid, *n*-hexane. From this suspension the appropriate amount, to get an optimal loading, is pipetted into a filtering funnel with vertical sides, filled with *n*-hexane. This suspension is then sucked through a 25 mm Nuclepore filter, 0.4 μm pore-size, supported by a glass filter.

Secondary electron images of algae cells and agglomerates were collected with an Integrated Microscope and X-ray microanalyzer system (IMIX) on a JEOL JSM-6300 electron microscope using an electron energy of 20 keV, a beam current of ca. 1 nA and typical magnification from 1000x to 9000x. A small collection of 30 SEM images: 24 images of individual algae cells and 6 images of cell agglomerates was acquired. Image processing was done using a set of techniques described in Part 1. Binary images of the cells and agglomerates were obtained by the correlation criteria based technique and the contour following technique was employed to extract the contours of the objects. The contour normalization and resampling was performed as above described. The shape descriptors having 64 coefficients were obtained for each object.

3.2.5. Results and discussion

A quantitative analysis of the population of individual cells and agglomerates was performed using hierarchical clustering. The dendrogram, representing the results of the hierarchical clustering is shown in Fig. 3.2.4. The presence of two classes of objects is evident from this dendrogram. One agglomerate was misclassified as belonging to the class of individual cells due to the nearly rounded shape of this agglomerate.

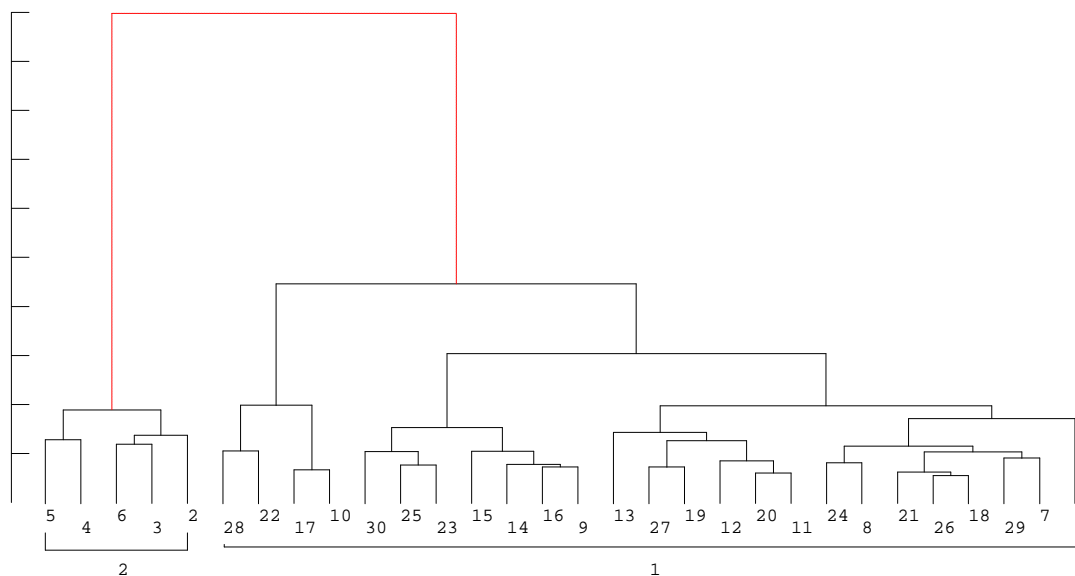


Fig. 3.2.4. Dendrogram showing the results of the hierarchical clustering of algae cells and cell agglomerates. Cell agglomerates are labeled from 1 to 6, individual cells are labeled from 7 to 30. Agglomerate #1 is misclassified.

Next the set of 30 shape descriptors was given to the trained network. The results of the corresponding outputs of the network are represented graphically in Fig. 3.2.5. For all algae cell agglomerates the network output is lower than 0.6 whereas for all individual cells the output is larger than 0.7.

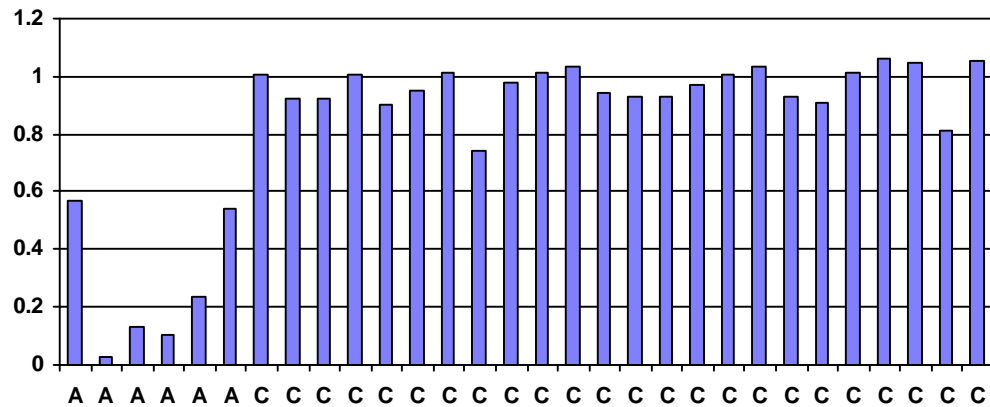


Fig. 3.2.5. Outputs of the trained network for the cells (C) and cell agglomerates (A).

3.2.6. Conclusions

The results of the analysis of SEM images of algae cells and their agglomerates show that the information about the shape of the objects, obtained in the form of the complex Fourier coefficients, is sufficient to be used for the identification of the individual cells and their agglomerates. The quantitative characterization of the entire collection of the objects can be performed by hierarchical clustering whereas the recognition of the objects belonging to the different classes can be performed by a trained neural network.

3.3. Classification of tabular grain silver halide microcrystals according to their shape

A method for the classification of individual tabular grain silver halide microcrystals according to their shape into one of three main classes, namely, hexagon, truncated triangle and regular triangle, is discussed. Principles of the functional approach to shape analysis, discussed in Part 2, are used. The method is based on the application of the Fourier descriptors of the microcrystals obtained from their SEM images. It is shown which Fourier descriptors describe different aspects of the shape of the microcrystals. Different classification algorithms, namely, crisp nearest prototype and nearest neighbor classifiers, fuzzy k -nearest neighbor and nearest prototype classifiers, are tested. It is found that the fuzzy k -nearest neighbor classifier produces the best results. Often a few microcrystals are overlapping in the SEM images and they form irregularly shaped ensembles. A method to extract the individual microcrystals from such ensembles is presented. The obtained results show the ability of the developed method to perform the identification of the microcrystals according to their shape.

3.3.1. Introduction

Tabular grain silver halide microcrystals are used as light sensitive material in modern photographic emulsion. They are produced in a reactor vessel by the precipitation reaction of Ag^+ with Cl^- , Br^- or I^- ions. Their shape, size and composition are determined by the growth (precipitation) conditions and in turn determine the properties and the quality of the photographic material. Under certain precipitation conditions a limited number of shapes are produced: regular triangles, regular hexagons and truncated triangles [3.3.1]. Fig. 3.3.1 shows SEM backscattered electron images of some typical crystals. Knowledge about the size and shape distribution of the microcrystals is important for the optimization of the precipitation process and for the study of the photographic properties of light sensitive films. This information can be obtained through analysis of individual microcrystals. Therefore the problem of classification of tabular silver halide microcrystals according to their shape is considered.

In the literature only few publications deal with this specific problem [3.3.1-3.3.3]. The methods described are based on the analysis of geometrical parameters of microcrystals obtained from their SEM images. The disadvantage of this approach is that it is very difficult to derive geometrical parameters from SEM image with sufficient accuracy. The method, described in [3.3.2], also requires manual work in order to extract these parameters. It is,

however, not necessary to base a classification on geometrical parameters, other suitable descriptors can be used as well. It has been shown [3.3.4] that many artificially generated and real shapes can be characterized by their Fourier power spectra. This idea is used in the present work. In addition different approaches to perform the classification based on the obtained parameters are tested, namely: the crisp and fuzzy k -nearest neighbor and the crisp and fuzzy one-nearest prototype classification algorithms.

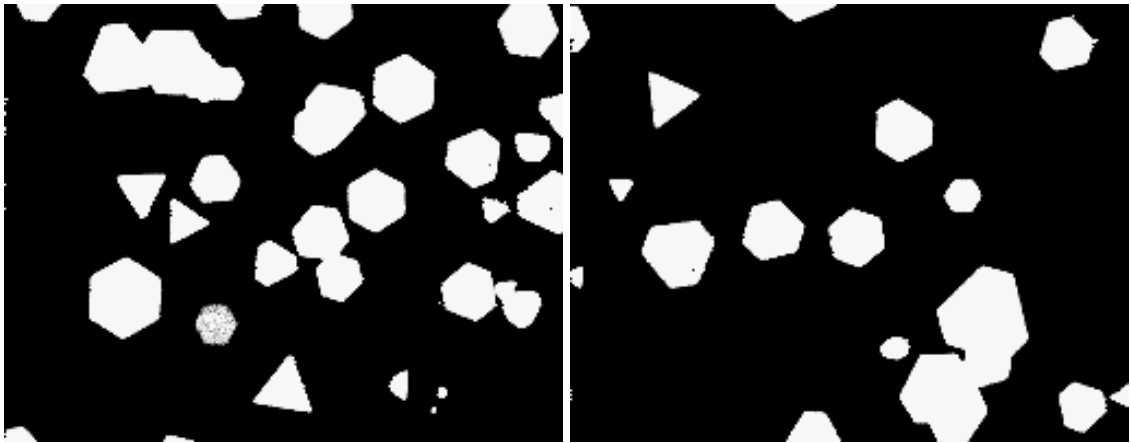


Fig. 3.3.1. Backscattered SEM images of tabular grain silver halide microcrystals.

3.3.2. Shape representation of the microcrystals

As it was mentioned above, under certain precipitation conditions a limited number of shapes is normally produced: regular triangles, regular hexagons and truncated triangles. Often few microcrystals are overlapping in the SEM images and they form irregularly shaped ensembles. For such type of objects it is convenient to use the idea of representation of figures by their contour functions introduced in Part 2. The radius-vector function $r(\varphi)$ is a suitable one. It can be easily computed from the contour's coordinates, it has a simple interpretation and can be easily analyzed for example by Fourier analysis. Of course, the function can be applied only to star-shaped figures, but for this particular problem only certain ensembles of overlapping silver halide microcrystals are not star-shaped. If the star-shape is violated, the object is immediately recognized as an ensemble of overlapping microcrystals. Of course, not all such ensembles can be recognized in this way.

For the given problem it is convenient to perform an analysis of the radius-vector function using its Fourier series expansion. The most important reason for this is the fact that the microcrystals are symmetric which is reflected by the radius-vector function in terms of periodicity. Thus, the radius-vector functions for the regular triangular and truncated

triangular microcrystals are periodical with the period $2\pi/3$ and for the hexagonal microcrystals they are periodical with the period $\pi/3$. It is shown in Part 2 that such periodicity is well reflected by the corresponding Fourier series coefficients. Thus, for the triangular microcrystals only the coefficients with indexes $3m$ ($m \in \mathbb{N}$) should be different from zero whereas for the hexagonal microcrystals only the coefficients with indexes $6m$ ($m \in \mathbb{N}$). Simulation (Fig. 3.3.2) confirms that radius-vector functions which give a good approximation of triangular and hexagonal shapes, can be obtained by inverse Fourier transformation using only the 3rd and 6th Fourier coefficients.

As seen, these coefficients are rather different for different shapes and they can serve as shape parameters suitable for microcrystals description and recognition. Of course, they cannot describe all possible shapes of microcrystals and especially not the shape of ensembles of overlapping microcrystals, but it was observed that the 2nd Fourier coefficient is different in the case of ensembles and it can serve as a suitable shape parameter to distinguish between ensembles and the rest of the microcrystals. Summarizing, the shape of the analyzed microcrystals can be adequately represented by only the three above mentioned Fourier coefficients obtained from the Fourier expansion of the radius-vector function.

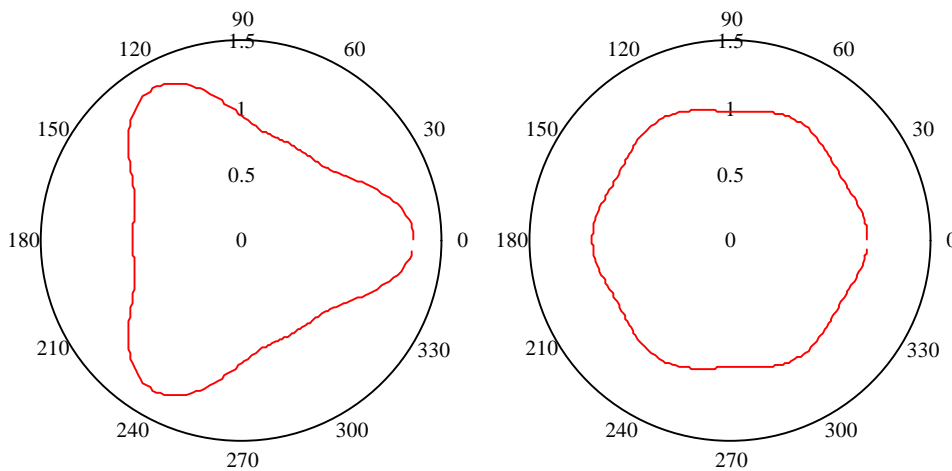


Fig. 3.3.2. Simulated radius-vector functions (shown in polar coordinates) are obtained by inverse Fourier transformation using 128 pairs of coefficients all equal to 0 except $a_0 = 1$, $a_3 = 0.25$ and $a_6 = 0.04$ for the function shown on the left side and $a_0 = 1$, $a_3 = 0.005$ and $a_6 = 0.035$ for the function shown on the right side.

Doing shape analysis, it is important to obtain invariant shape features. It has been shown in Part 2 which classical invariant shape parameters can be obtained from Fourier coefficients. However, for this particular problem it is more convenient to use invariant parameters, obtained in the following way.

First, preprocessing of the radius-vector function eliminates the size difference between microcrystals. It can be done dividing $r(\varphi)$ by $\max_{0 \leq \varphi \leq 2\pi} r(\varphi)$.

Second, squared harmonic amplitudes can serve as shape parameters invariant to orientation and reflection. Examples of squared Fourier harmonic amplitudes obtained in this way are shown in Fig. 3.3.3 for differently shaped microcrystals.

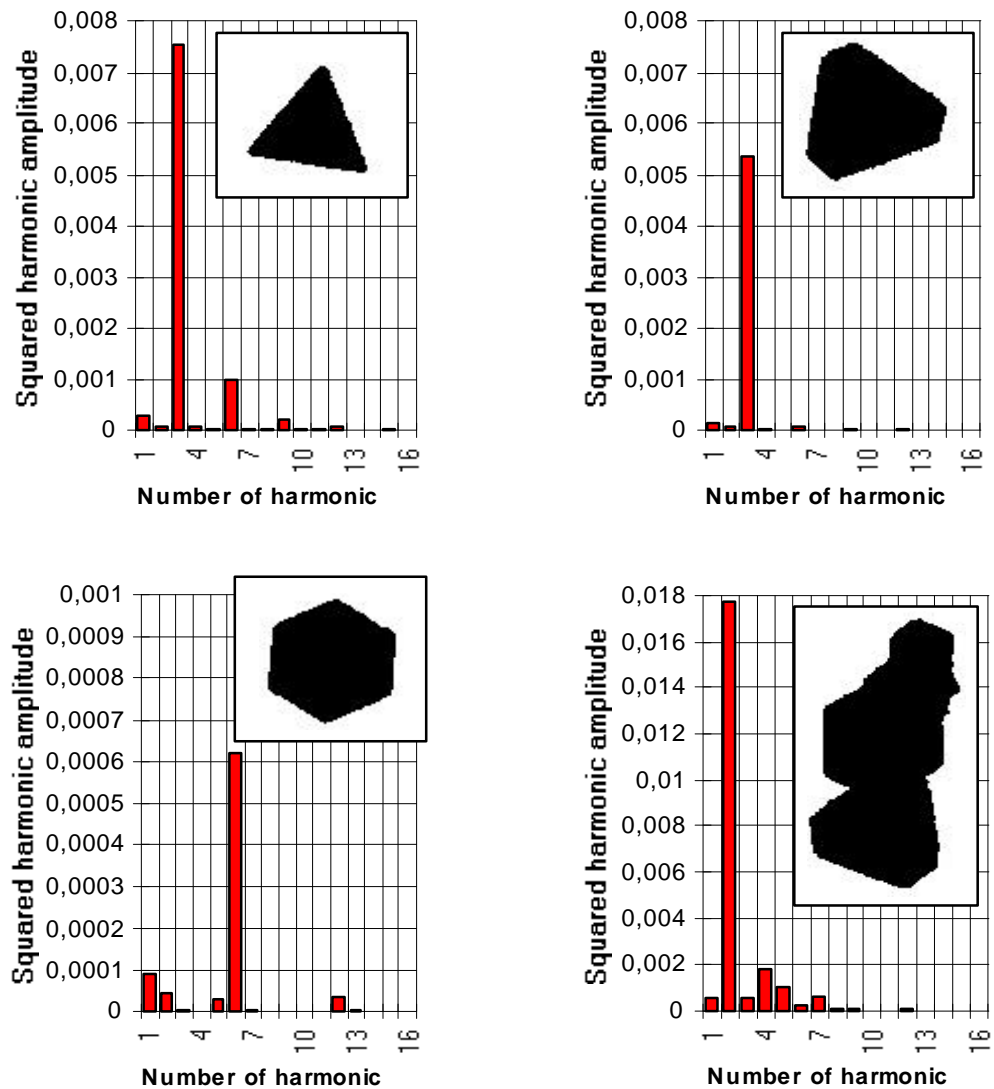


Fig. 3.3.3. Differently shaped microcrystals and corresponding squared harmonic amplitudes.

The invariant shape parameters used in the present study for the classification of differently shaped microcrystals are the squared amplitudes of the second, third and sixth harmonics obtained by the Fourier series expansion of the radius-vector function of the microcrystals.

3.3.3. Reconstruction of the shape of overlapping microcrystals

It has been shown that in some cases ensembles of overlapping microcrystals can be recognized by the fact that their radius-vector function is multivalued. Later it will be shown how ensembles, unrecognized at this stage of analysis, can be recognized during the general classification procedure, developed in this work. To obtain statistically correct results, the microcrystals which form these ensembles, also should be taken into account. Thereby, there is a need to perform an extraction of overlapping microcrystals from the ensembles. The segmentation procedure, developed in this work and described below, allows to obtain the contours of overlapping microcrystals which then can be analyzed in the usual way starting from the calculation of the corresponding radius-vector functions. The method is based on the analysis of geometrical information obtained from the position of the vertexes of an ensemble of overlapping microcrystals and is independent of the orientation, location, reflection and size.

The main steps of the reconstruction procedure are illustrated in Fig. 3.3.4.

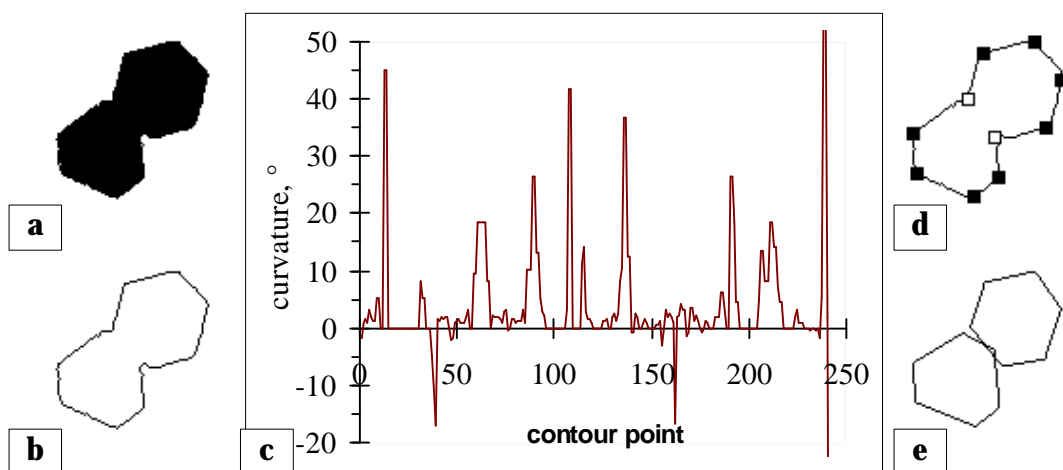


Fig. 3.3.4. Reconstruction procedure: **a)** binary image; **b)** extracted contour; **c)** estimated curvature at each point of the contour; **d)** vertexes belonging to hexagonal microcrystals are marked in black; **e)** contours of reconstructed microcrystals.

After the contour of the ensemble of overlapping microcrystals is extracted (Fig. 3.3.4b) the curvature at every point of the contour is determined (Fig. 3.3.4c) using the so-called median differencing technique [3.3.5]. The points of maximal curvature of the contour serve as the vertexes of the ensemble of overlapping microcrystals.

Actually, many local extremes in the curvature plot are observed in Fig. 3.3.4c. Most of them are caused by the digital nature of the contour and local imperfections in the crystals (noise) and only few correspond to the real vertexes. To separate them from the noise a threshold value of the curvature equals to 15° was experimentally found. The vertexes found in this way are marked by boxes in Fig. 3.3.4d. Some of them are also recognized as belonging to hexagonal microcrystals and are shown by filled boxes. Finally, Fig. 3.3.4e shows the reconstructed contours of the hexagonal and the truncated triangular microcrystals. The rules, used to perform such reconstruction, are explained below.

Extraction of hexagonal and truncated triangular microcrystals

Both hexagonal and truncated triangular silver halide microcrystals have all vertexes equal to 120° . A regular hexagon has equal sides whereas a truncated triangle has sides of two different lengths. These properties and the parallelity of the opposite sides can be used to reconstruct partially overlapping microcrystals of this category.

The values of vertexes are determined with the cosine theorem. If the value is between $\alpha_l = 105^\circ$ and $\alpha_u = 135^\circ$ the corresponding vertex is marked. The limiting values of α_l and α_u were determined experimentally. With such limits vertexes due to noise and vertexes which do not belong to hexagonal or truncated triangular microcrystals are eliminated. The ordered sequences of marked vertexes are extracted and analyzed separately in order to reconstruct the entire shape of hexagonal or truncated triangular microcrystals, if possible. If the vertex detection and marking procedures were correct the sequences having 6, 5, 4, 3, 2 or 1 vertexes are expected to be obtained. Of course, it is impossible to reconstruct the shape of a hexagonal or truncated triangular microcrystal having only one vertex. In case of 2 vertexes only the shape of a regular hexagon can be reconstructed but without faith in the true shape. The contour of regular hexagonal and truncated triangular microcrystals can be reconstructed with sufficient accuracy having 3, 4, 5 or 6 vertexes.

With 6 vertexes, the shape of the hexagonal or truncated triangular microcrystal can be reconstructed by sequentially connecting all of them (Fig. 3.3.5a). Two real examples of such reconstruction are shown in Fig. 3.3.5b.

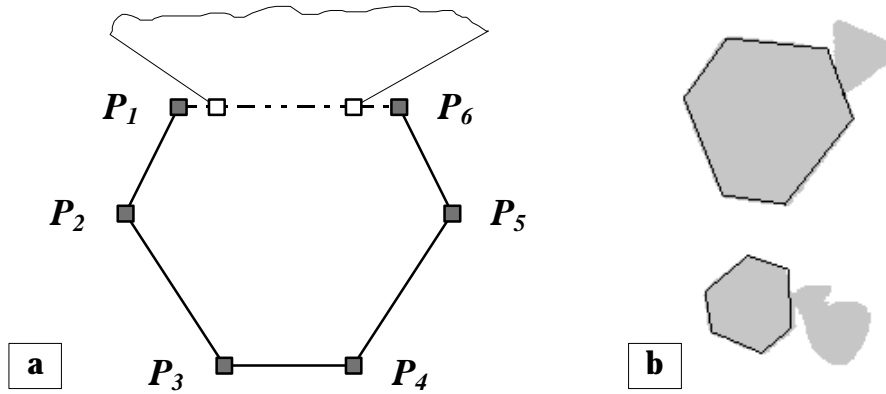


Fig. 3.3.5. a) rule used to reconstruct the contour of a hexagonal or a truncated triangular overlapping microcrystal when 6 vertexes are found; b) examples of overlapping microcrystals and reconstructed contours applying this rule.

Having 5 vertexes, the contour of a hexagonal or truncated triangular microcrystal can be reconstructed by adding the 6th vertex in the following way. Let P_1, P_2, P_3, P_4 and P_5 be an ordered sequence of vertexes found to be belonging to a hexagonal or truncated triangular microcrystal and P_0 and P_6 vertexes before P_1 and after P_5 , respectively, not belong to the microcrystal (Fig. 3.3.6a).

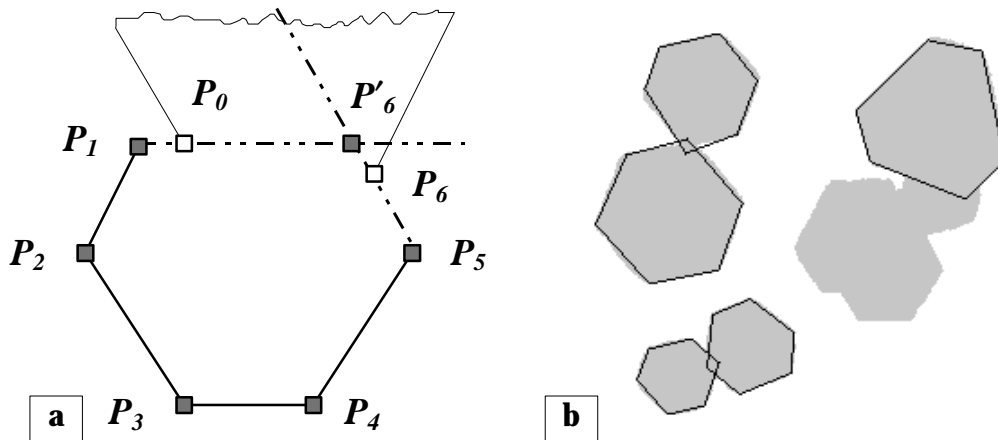


Fig. 3.3.6. a) rule used to reconstruct the contour of a hexagonal or a truncated triangular overlapping microcrystal when 5 vertexes are found; b) examples of overlapping microcrystals and reconstructed contours applying this rule.

The 6th vertex P'_6 of the microcrystal is at the interception of the lines P_1P_0 and P_5P_6 . The coordinates of this point can be found as the solution of the system of equations

$$\begin{cases} \frac{y - y_1}{y_0 - y_1} = \frac{x - x_1}{x_0 - x_1} \\ \frac{y - y_5}{y_6 - y_5} = \frac{x - x_5}{x_6 - x_5} \end{cases}$$

representing the lines P_1P_0 and P_5P_6 passing through the points $P_1(x_1, y_1)$, $P_0(x_0, y_0)$ and $P_5(x_5, y_5)$, $P_6(x_6, y_6)$, respectively. Finally, having 6 vertexes the contour of the microcrystal can be reconstructed as described above. Some real examples of such reconstruction are shown in Fig. 3.3.6b.

If only 4 vertexes of a hexagonal or truncated triangular microcrystal are available the following procedure can be used for the reconstruction. Let P_1 , P_2 , P_3 and P_4 be an ordered sequence of points representing the found vertexes of a hexagonal or truncated triangular microcrystal and P_0 and P_5 vertexes before and after the given sequence, respectively (Fig. 3.3.7a).

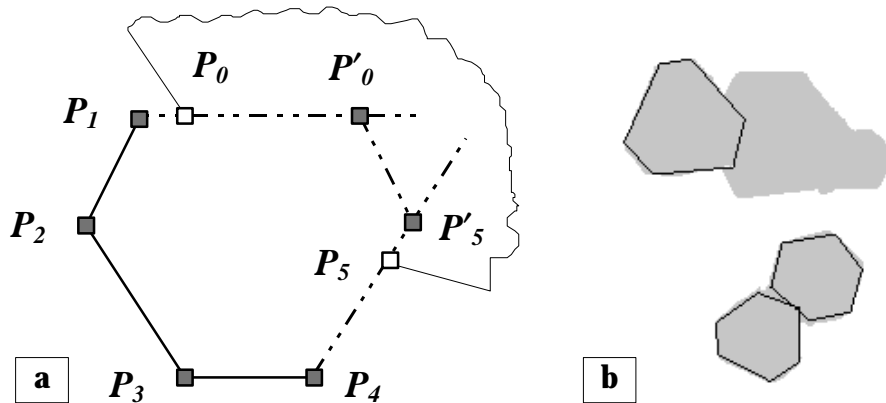


Fig. 3.3.7. a) rule used to reconstruct the contour of a hexagonal or a truncated triangular overlapping microcrystal when 4 vertexes are found; b) examples of overlapping microcrystals and reconstructed contours applying this rule.

The 5th vertex of the microcrystal P'_5 (to be found) belongs to the line P_4P_5 and the length of $P_4P'_5$ is equal to the length of the side P_2P_3 . So, its coordinates (x'_5, y'_5) can be calculated using the coordinates of the points P_4 and P_5 as $x'_5 = x_4 + l(x_5 - x_4)/d$ and $y'_5 = y_4 + l(y_5 - y_4)/d$ where l is the length of P_2P_3 and d is the length of P_4P_5 . The 6th vertex of the microcrystal, P'_0 , belongs to the line P_1P_0 and the length of $P_1P'_0$ is also equal to the length of the side P_2P_3 . Its coordinates can be found in a similar way using the coordinates of the points P_1 and P_0 . Some real examples of such reconstruction are shown in Fig. 3.3.7b.

Having only 3 vertexes of a hexagonal or truncated triangular microcrystal, the remaining 3 can be found in the following way. Let P_1 , P_2 and P_3 be an ordered sequence of points representing the vertexes of a hexagonal or truncated triangular microcrystal and P_0 and P_4 vertexes before and after this sequence (Fig. 3.3.8a).

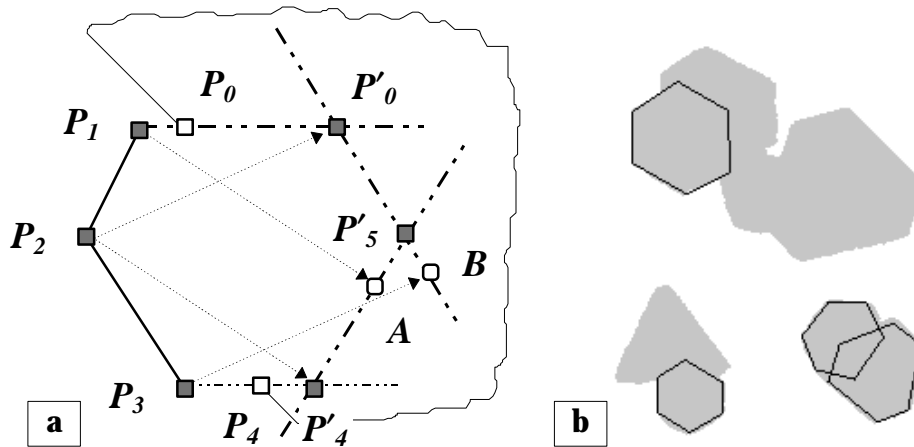


Fig. 3.3.8. a) rule used to reconstruct the contour of a hexagonal or a truncated triangular overlapping microcrystal when 3 vertexes are found; b) examples of overlapping microcrystals and reconstructed contours applying this rule.

Two out of three remaining vertexes P'_0 and P'_4 of the microcrystal can be found in a similar way as described for the 4 vertexes case. The 6th vertex P'_5 can be found as the interception of two lines parallel to lines P_1P_2 and P_2P_3 which cross the points P'_4 and P'_0 , respectively. This interception can be found in a similar way as described for the case of 5 vertexes where the line which passes the point P'_4 and is parallel to the P_1P_2 also passes the point A with coordinates $(x_1 + (x'_4 - x_2), y_1 + (y'_4 - y_2))$. Similarly, the line is passing the point P'_0 and is parallel to the side P_2P_3 also passes the point B with coordinates $(x_3 + (x'_0 - x_2), y_3 + (y'_0 - y_2))$. Some real examples of such reconstruction are shown in Fig. 3.3.8b.

When only 2 vertexes of a hexagonal or truncated triangular microcrystal were found a regular hexagonal microcrystal having all sides equal can be reconstructed. Let P_1 and P_2 be an ordered sequence of points representing the vertexes of a microcrystal, P_0 and P_3 be one vertex before the given sequence and one vertex after the given sequence (Fig. 3.3.9a). Two vertexes P'_0 and P'_3 of the microcrystal can be found in the way similar to the case when 4 vertexes are available. The remaining 2 vertexes P'_4 and P'_5 can be defined using the property of central symmetry of a regular hexagon.

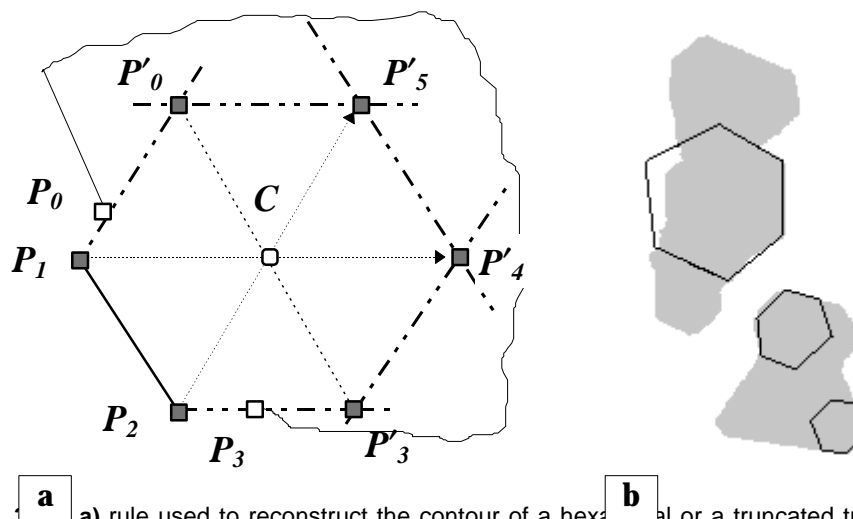


Fig. 3.3.9 a) rule used to reconstruct the contour of a hexagonal or a truncated triangular overlapping microcrystal when 2 vertexes are found; b) examples of overlapping microcrystals and reconstructed contours applying this rule.

The center of symmetry C of the hexagon has coordinates $((x'_0 + x'_3)/2, (y'_0 + y'_3)/2)$. The point P'_5 belongs to the line P_2C and the distance from the point C to the point P'_5 is equal to the distance from the point P_2 to the point C . Thus coordinates of the point P'_5 can be found using equations similar to that used in the case when 4 vertexes are available. The last vertex P'_4 is defined in a similar way. Of course, in many cases this reconstruction will be wrong because there is no guaranty that the considered microcrystal is indeed a hexagon - it can be a truncated triangular microcrystal as well. Moreover, it is not always possible to check the correctness of the reconstruction even by visual inspection. Some real examples of such reconstruction are shown in Fig. 3.3.9b. Clearly a reconstruction based on only two vertexes is often subject to large errors.

Extraction of triangular microcrystals

The contours of partially overlapping triangular microcrystals also can be extracted based on their geometrical properties. This type of silver halide microcrystals are regular triangles with equal sides and vertexes of 60° .

The limiting angles for the detection of triangular microcrystals were $\alpha_l = 40^\circ$ and $\alpha_u = 80^\circ$. All continuous ordered sequences of vertexes previously selected as belonging to triangular microcrystals are extracted and analyzed separately in order to reconstruct the shapes. If the vertex detection and marking procedure is done correctly sequences of vertexes having 3, 2 or 1 points are expected to be obtained.

When a sequence has only 1 vertex obviously it is impossible to reconstruct the

corresponding triangular microcrystal correctly. If a sequence contains 3 points the contour of the microcrystal can be reconstructed by sequentially connecting its vertexes. When only two vertexes are available the 3rd vertex of the triangular microcrystal can be determined as follows. Let P_1 and P_2 represent two real vertexes of a triangular microcrystal and P_0 and P_3 two vertexes which were detected in the ensemble: P_0 is located before vertex P_1 , P_3 is located after vertex P_2 (see Fig. 3.3.10a). The coordinates of the 3rd vertex P'_3 , belonging to the microcrystal, is found as the coordinates of the point of the intersection of the lines P_1P_0 and P_2P_3 in the way similar to that described above for the case of a hexagonal microcrystal having 5 vertexes. Some real examples of such reconstruction are shown in Fig. 3.3.10b.

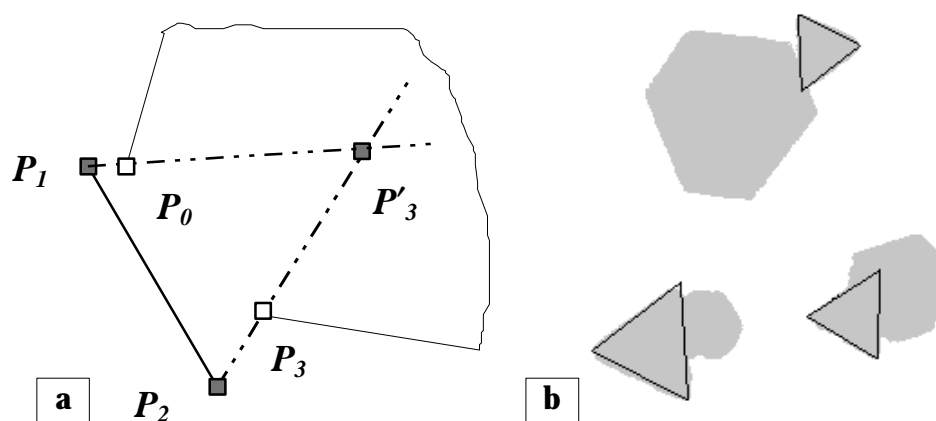


Fig. 3.3.10. a) rule used to reconstruct the contour of a triangular overlapping microcrystal when 2 vertexes are found; b) examples of overlapping microcrystals and reconstructed contours applying this rule.

3.3.4. Classification of microcrystals via their shape descriptors

The microcrystal's shape is represented by a point in the 3D space of the 2nd, 3rd and 6th squared harmonic amplitudes of the corresponding Fourier coefficients obtained by expanding the radius-vector functions into Fourier series. Thus, the problem of recognition of individual silver halide microcrystals is converted to the problem of multidimensional pattern classification. Different modifications of the nearest neighbor classification algorithm [3.3.6] were tested in order to find the best solution to this problem.

Nearest neighbor classification algorithms

Let z_1, z_2, \dots, z_c be a set of c prototype vectors representing the c classes, for example the centers of the classes in which each member is represented by a point in the 3D space of the 2nd, 3rd and 6th squared harmonic amplitudes. The *crisp one-nearest prototype classifier* assigns an input sample vector y to the class of its nearest neighbor prototype.

Let x_1, x_2, \dots, x_q be a set of vectors representing the q labeled samples from the c classes. The *crisp nearest neighbor classifier* assigns an input sample vector y to the class of its nearest neighbor. This idea can be extended to the k nearest neighbors. But, when more than one neighbor is considered, the possibility that there will be a tie among classes with a maximum number of neighbors in the group of k nearest neighbors exists. The usual way of handling this problem is to assign the sample vector to the class, of those classes that tied, for which the sum of distances from the sample to each neighbor in the class is minimal.

The idea of one-nearest prototype classifier can be extended to the *fuzzy one-nearest prototype classifier*. Such classifier assigns a membership of a sample vector y to the i^{th} class ($i = 1, 2, \dots, c$) rather than assigning vector y to a particular class i . The basis of the algorithm is to assign a membership $u_i(y)$ as a function of the vector's distance from all prototypes:

$$u_i(y) = \frac{1}{\|y - z_i\|^{\frac{2}{m-1}}} \left(\sum_{t=1}^c \frac{1}{\|y - z_t\|^{\frac{2}{m-1}}} \right)^{-1}.$$

The *fuzzy k -nearest neighbor classifier* assigns a membership value of a sample vector y in the class i as a function of the vector's distance from its k nearest neighbors. Let $u_i(y)$ be the assigned membership of the vector y (to be computed), and u_{ij} is the membership in the i^{th} class of the j^{th} vector ($j = 1, 2, \dots, q$) of the labeled sample set, then u_{ij} can be computed in the following way based on the k -nearest neighbor rule. The k' (not k of the classifier)-nearest neighbors to each j^{th} sample (say, a sample from a class t) are found and their membership in each i^{th} class is assigned according to the following equation:

$$u_{ij} = \begin{cases} 0.51 + 0.49 \frac{n_i}{k'} & \text{if } t = i \\ 0.49 \frac{n_i}{k'} & \text{otherwise} \end{cases}$$

where the value n_i is the number of the neighbors found which belong to the i^{th} class. Finally, $u_i(y)$ is computed according to the following equation:

$$u_i(y) = \sum_{j=1}^k \frac{u_{ij}}{\|y - x'_j\|^{\frac{2}{m-1}}} \left(\sum_{j=1}^k \frac{1}{\|y - x'_j\|^{\frac{2}{m-1}}} \right)^{-1}$$

where $\{x'_j\}$ ($j = 1, 2, \dots, k$) is the set of k nearest neighbors of the given vector y . The parameter m determines how heavily the distance is weighted when calculation each neighbor's contribution to the membership value. As m increases, the neighbors are more evenly weighted, and their relative distances from the point being classified have less effect.

Labeled samples and prototypes

The k -nearest neighbor classification algorithms require sets of labeled samples (or prototypes) which represent different classes. This set was generated by analyzing the data obtained from a subset of collected microcrystals. Minimal and maximal values of the squared amplitudes of the 2nd, 3rd and 6th harmonics were determined for each class of microcrystals (Table 3.3.1). Combining these values, the 8 prototypes for each class of microcrystals were obtained. One additional prototype for each class of microcrystals was obtained by using the average values of the minimal and maximal squared amplitudes of the 2nd, 3rd and 6th harmonics.

microcrystals	2 nd harmonic			Squared amplitudes of the 3 rd harmonic			6 th harmonic		
	min	max	average	min	max	average	min	max	average
triangles	-0	0.0004	0.0002	0.0069	0.0081	0.0075	0.0004	0.0010	0.0007
truncated triangles	-0	0.0004	0.0002	0.0008	0.0067	0.0037	0.0000	0.0004	0.0002
hexagons	-0	0.0002	0.0001	-0	0.0004	0.0002	0.0003	0.0006	0.0005
overlapping microcrystals	0.0044	0.0293	0.0168	0.0001	0.0045	0.0023	-0	0.0005	0.0003

Table 3.3.1. Minimal, maximal and average values of the 2nd, 3rd and 6th squared harmonic amplitudes obtained from a subset of the experimental data set. The set of labeled samples (prototypes) for the crisp and fuzzy 4-nearest neighbor classifiers was obtained by combining only minimal and maximal values. Average values of the 2nd, 3rd and 6th squared harmonic amplitudes were used as set of prototypes for the crisp and fuzzy one-nearest prototype classifiers.

Thus each class of differently shaped microcrystals is represented by 9 points in a 3D space

formed by the squared amplitudes of the 2nd, 3rd and 6th harmonics. Such artificially generated labeled samples allowed to divide the 3D space into 'class subspaces' which are bounded by the parallelepipeds formed by the first 8 points for each class (Fig. 3.3.11).

For the crisp k -nearest neighbor and the fuzzy k -nearest neighbor classifiers all 9 points of each class were used as the set of labeled samples. For the crisp one-nearest prototype and the fuzzy one-nearest prototype classifiers only the central points, i.e. the average values of the minimal and maximal squared amplitudes, were used as the set of labeled prototypes.

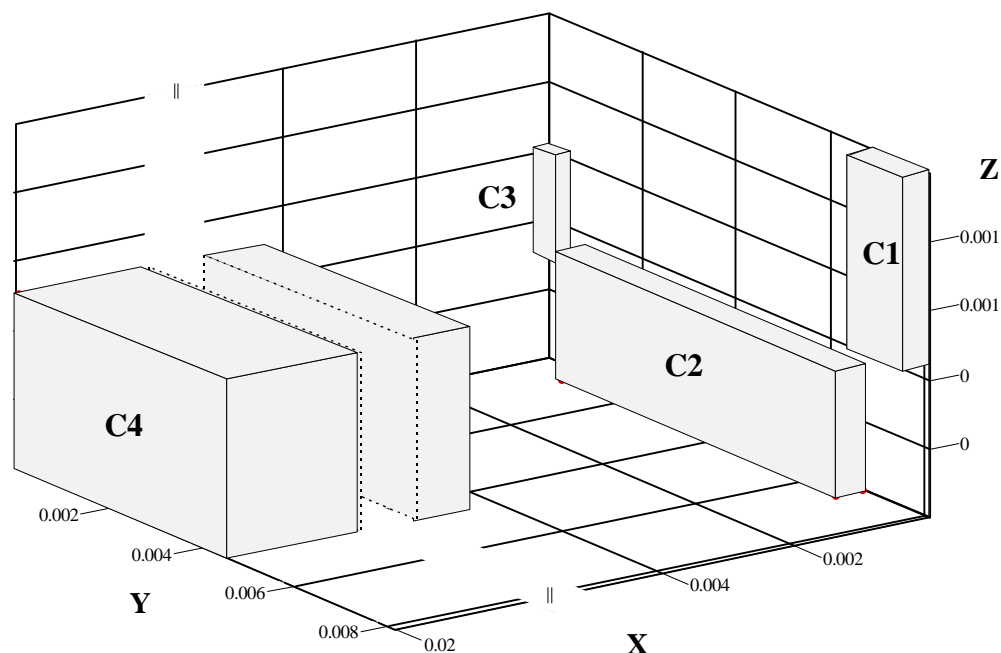


Fig. 3.3.11. A 3D space formed by the squared amplitudes of the 2nd (X axes), 3rd (Y axes) and 6th (Z axes) harmonics. The corners of the parallelepipeds correspond to the 8 prototypes for each class of microcrystals (C1 - triangular microcrystals, C2 - truncated triangular microcrystals, C3 - hexagonal microcrystals, C4 - ensembles of overlapping microcrystals). The 3D space is divided by these 4 parallelepipeds into 4 separated 'class subspaces'.

3.3.5. Experimental

Backscattered electron images of tabular silver halide microcrystals were acquired with an Integrated Microscope and X-ray microanalyzer (IMIX) system on a JEOL JSM-6300 electron microscope using an electron energy of 20 keV, a beam current of ca. 1 nA and typical magnification ca. 3000x. A liquid nitrogen cooling stage was used to decrease the

deformations of the sample because the photographic silver halide microcrystals are sensitive to irradiation. The operation temperature at the electron microscope is as low as possible i.e. -186° C. At this temperature no reaction was visible in the scanning electron images. More details about the samples used in this work, the sample preparation and image acquisition techniques can be found in [3.3.1].

Acquired images were binarized using the correlation criteria based technique described in Part 1. Next, the area (the number of pixels belonging to an object) of all microcrystals was calculated and only microcrystals with the area larger than a predefined value (300 pixels) were selected for analysis. Finally, contours of selected microcrystals were extracted from their binary images by the crack following technique described in Part 1 and stored as a list of coordinates. The following was done in order to obtain invariant shape parameters. The center of mass of a microcrystal was used as the origin to obtain the radius-vector function. It was calculated as the sum of the corresponding contour's coordinates x and y divided by the total number of points on the contour. The 360 radii, measured from the center of mass to the contour points with step 1° were obtained for the microcrystal and normalized to the largest radius in order to obtain the size invariant shape parameters. If some radial vectors are multivalued (i.e. the shape is re-entrant) the corresponding object is considered as belonging to the class of overlapping microcrystals. Otherwise, the radius-vector function is expanded into Fourier series. The microcrystal shape parameters used for representation and classification are the 2nd, 3rd and 6th squared harmonic amplitudes of the corresponding Fourier coefficients. All calculations were performed with software developed as part of this thesis.

3.3.6. Results and discussion

Results of the classification of differently shaped microcrystals by the crisp 4-nearest neighbor and the crisp one-nearest prototype classifiers are summarized in Table 3.3.2. Some examples of results of classification by these algorithms are shown in Table 3.3.3. The parameter $k = 4$ was found to be the most suitable one after thorough analysis of all cases for k equals 1 to 9. It was observed that in most cases the first 4 nearest neighbors of any point corresponding to the microcrystal shape belong to one class.

The crisp 4-nearest-neighbor classifier gave good results. At the same time the use of the crisp one-nearest prototype classifier results in a large number of miss-classifications, especially of truncated triangles and overlapping microcrystals. These results are expected because triangles and hexagons form small, compact clusters in the 3D space of the squared amplitudes of the 2nd, 3rd and 6th harmonics whereas truncated triangles and especially ensembles of overlapping microcrystals show a large variety of shapes and therefore form

large clusters.

type of microcrystals	total number of microcrystals	correctly classified by the	
		crisp 4-nearest-neighbour classifier	crisp one-nearest prototype classifier
triangles	12	100%	100%
truncated triangles	25	100%	32%
hexagons	16	100%	100%
ensembles of overlapping microcrystals	12	92%	33%

Table 3.3.2. Summary of classification of 65 microcrystals by the crisp 4-nearest neighbor and one-nearest prototype classifiers.

Although the crisp 4-nearest neighbor classifier gives good results, the advantage of using fuzzy k -nearest neighbor and fuzzy k -nearest prototype classifiers can be understood by examining a microcrystal which has a truncated trapezoidal shape. The crisp classifier will classify it to one of the 4 classes even if the truncated trapezoid does not belong to them. At the same time the fuzzy 4-nearest neighbor classifier ($m = 3$) gives values of the membership for the truncated trapezoid in every class. These values however are not high enough for making the decision about its belonging to any class. Moreover the fuzzy classifier allows us to do more precise classification of triangles. The triangular microcrystals are defined as microcrystals whose length of the short edges is smaller than 10% of that of the long one [3.3.1]. According to human observation it is not always obvious to classify some microcrystals to the class of triangles or truncated triangles. The fuzzy 4-nearest neighbor classifier gives in these cases values of membership in the class of triangles lower than 0.9. This fact can be used for recognizing such intermediate microcrystals.

The fuzzy one-nearest prototype classifier has the same disadvantage as crisp one-nearest prototype classifier - it often misclassifies truncated triangles and overlapping microcrystals.

For the experimental data set considered, the fuzzy 4-nearest neighbor classifier gave highest membership values of all overlapping microcrystals in their own class and only for one overlapping microcrystal it gave a high value of membership for the class of hexagonal microcrystals (0.81). Since this class is represented by a compact small cluster it is possible to specify the lowest value of membership of belonging to this class as 0.9. Actually, the lowest values of memberships of belonging for the remaining classes can be specified as well. For triangles and hexagons this value is 0.9. For truncated triangles and overlapping microcrystals

this value is 0.7. A microcrystal is unclassified if it has memberships values in every class lower than the specified lowest values. One additional rule is used to classify a microcrystal as an (intermediate) truncated triangle: it must have a membership value in the class of triangles between 0.7 and 0.9 and a membership value in class of truncated triangles larger than 0.1. Some examples of results of classification by different algorithms are shown in Table 3.3.3.

Differently shaped microcrystals	Results of classification by crisp		Membership values, obtained by fuzzy 4-nearest neighbor classifier				Membership values, obtained by fuzzy one-nearest prototype classifier				Finally classified as
	4-nearest neighbor classifier	1-nearest prototype classifier	C1	C2	C3	C4	C1	C2	C3	C4	
	triangle	triangle	1	0	0	0	0.88	0.07	0.04	0.1	triangle
	triangle	triangle	0.88	0.12	0	0	0.8	0.12	0.06	0.02	(intermediate) truncated triangle
	truncated triangle	truncated triangle	0.12	0.88	0	0	0.34	0.46	0.15	0.05	truncated triangle
	truncated triangle	hexagon	0	0.88	0.12	0	0.12	0.31	0.53	0.04	truncated triangle
	hexagon	hexagon	0	0	1	0	0.03	0.06	0.89	0.01	hexagon
	ensemble of overlapping micro-crystals	ensemble of overlapping micro-crystal	0	0.22	0	0.78	0.21	0.3	0.34	0.16	ensemble of overlapping micro-crystals
	ensemble of overlapping micro-crystals	hexagon	0	0.42	0.03	0.54	0.17	0.29	0.44	0.1	unknown

Table 3.3.3. Comparison of results of classification by different algorithms. Column 'Finally classified as' obtained from classification by fuzzy 4-nearest neighbor classifier using the additional rules for the classification of truncated triangles, described in the text. The same abbreviations as in Fig. 3.3.11 were used.

The accurate classification of the shape of tabular grain silver halide microcrystals is possible only with the fuzzy 4-nearest neighbor classifier. The three other classification algorithms,

examined in the present work, produce misclassifications. An example of results of the classification by the proposed algorithm is shown in Fig. 3.3.12.

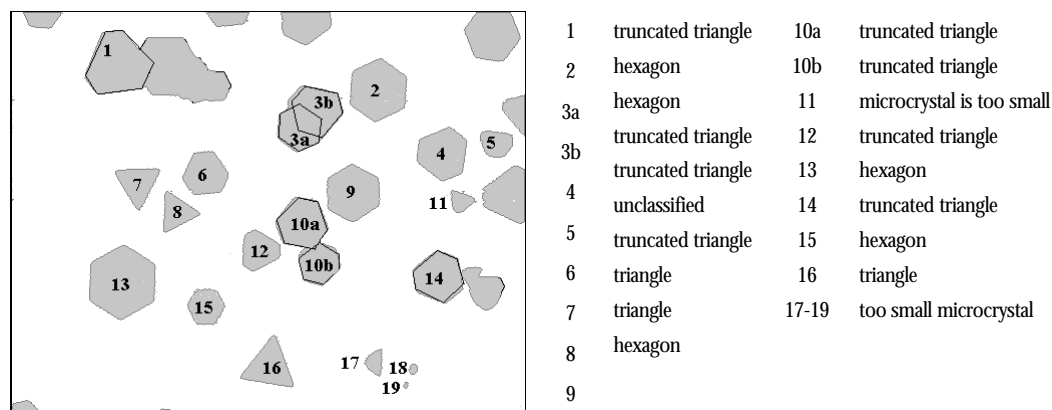


Fig. 3.3.12. A typical backscattered electron image (after preprocessing) of silver halide microcrystals. Labeled microcrystals are classified according to their shape as show in the table.

3.3.7. Conclusions

A method for the classification of tabular grain silver halide microcrystals according to their shape is described. Shape descriptors, obtained from the Fourier power spectra, are used to describe the shape of microcrystals. Fourier power spectra are obtained from the radius-vector functions. The classification of the shapes is based on nearest neighborhood algorithms. Results of the classification by 4 different algorithms are compared and the fuzzy 4-nearest neighbor classifier was found to be the most appropriate one. In addition, a reconstruction procedure of the contours of microcrystals from ensembles of overlapping microcrystals is developed. The method can be used for the control of the precipitation process and for the study of the photographic properties of light sensitive materials.

3.4. On fractal dimension calculation

In section 3.1 shown how fractal concept was successfully applied to the analysis of the shape of aerosol particles. The method was found to be robust to the selection of the threshold value used to discriminate the particles from the background. To some extent the change of the threshold value can be interpreted as a making a slice of the particle at different height. However, a few problems related to the calculation of the fractal dimension by the 'hand and dividers' method were encountered the answers to which could not be found in the literature. One of them is the need to perform a visual inspection of the log-log plots in order to find the best straight line intervals to be fitted. Another is the presents of random errors in the approximated perimeter as well as in the yardstick size used to approximate the perimeter. The aim of this part is to examine these problems in more details and to show what kind of effects can be observed.

3.4.1. 'Hand and dividers' method: theory

There are a variety of methods to estimate the fractal dimension developed over the past decade [3.4.1]. However, the oldest, classical 'hand and dividers' method is one of the most frequently used in practice. 'Hand and dividers' method (also called 'structured walk technique' or 'yardstick method') is a precise method for manual determination of fractal dimension of planar curves on paper. It uses the following mathematical model. Consider the boundary B of a figure. An arbitrary point S on the boundary is selected and the point S_1 , located from S on the distance r_1 , is found traveling along the boundary in one direction. The process is repeated starting from S_1 until the entire boundary is scanned and the number $N(r_1)$ of intervals of length r_1 is counted. It is clear that the discs corresponding to the circles having origins in S_1, S_2, \dots and radii r_1 , cover B completely. Thus $N(r_1)$ can be interpreted as an approximation of the disc numbers $M_r(B)$ in the last but one equation (Part 2 section 2.2.1) from which the fractal dimension can be obtained. The procedure is repeated for widths r_1, r_2, \dots with $r_1 > r_2 > \dots$. Then approximations $l(r_i)$ for the length of B are obtained as $l(r_i) = r_i N(r_i)$. If D is the fractal dimension of the boundary B , then the following equation can be written:

$$-D = \lim_{r \rightarrow 0} \sup \frac{\log M_r(B)}{\log r}.$$

For small r this corresponds to

$$-D = \frac{\log M_r(B)}{\log r} \text{ or } M_r(B) = r^{-D}.$$

Finally this can be rewritten as $l(r) = cr^{1-D}$ where c is a scaling factor, or as $\log l(r) = \log c + (1-D)\log r$ which has the form of a regression line $y = ax + b$ from which an estimate of D can be obtained by calculating the slope a .

The 'hand and dividers' method has an interesting history. It was originally developed by Richardson in his attempt to answer the question "How long is the coastline of Great Britain" [3.4.2]. The answer to this question essentially seems to depend on the yardstick size used to measure the length of the coastline. Richardson observed that if the measured coastline was plotted against the size of the yardstick, λ , using logarithmic axes (Richardson plot), the result was a straight line. Furthermore, the slope of the line was different for different boundaries. More irregular coastlines, as judged by human observers, always result in a line with a higher slope. The slope is negative, since the largest value for the coastline length is obtained with the shortest yardstick. The magnitude of the slope of the line is between zero and one. Mandelbrot showed [3.4.3] that fractal dimension of the coastline is just this magnitude plus 1, the topological dimension of a line.

3.4.2. 'Hand and dividers' method: practice

Descriptions of many computer implementations of 'hand and dividers' method can be found in the literature [3.4.1, 3.4.4-3.13]. The general procedure is the following. The contour of an object is obtained using a boundary following technique, resulting in a set of contour points $\{(x_i, y_i)\}$. In image analysis there are several definitions of boundary; the so-called inner 8-boundary is often used in fractal analysis [3.4.13]. Having the boundary of the projection of the object the corresponding Richardson plot is obtained by performing perimeter estimation for different yardstick sizes. The length of the yardstick λ usually varies between 0.001 and 0.5 times the maximum Feret diameter. The corresponding Richardson plot is formed by plotting the *perimeter* versus the *average yardstick size* using logarithmic axes. From this plot the fractal dimension is obtained by the least-squares line fitting.

For a given yardstick size λ the perimeter is determined as follows. Starting at some arbitrary contour point (x_s, y_s) the next point on the contour (x_n, y_n) in clockwise direction is located which has a distance

$$d_j = \sqrt{(x_s - x_n)^2 + (y_s - y_n)^2}$$

as close as possible to λ . This point is then used to locate the next point on the contour that satisfies this condition. The process is repeated until the initial starting point is reached. The perimeter is the sum of all distances d_j including the distance between the last located point and the starting point. The average yardstick size is the sum of all distances d_j (excluding the distance between the last located point and the starting point) divided by the number of

points found.

The above described algorithm is referred to in the literature as the 'hybrid' method [3.4.4] with only one important difference. In the original version of the algorithm the average yardstick size is defined as the perimeter divided by the number of steps, thus taking into account the distance between the last located point and the starting point which can be significantly different from the initial yardstick size especially for large λ . In the algorithm described here this problem is avoided.

3.4.3. Problems associated with the 'hand and dividers' method

A problem was observed using the 'hand and dividers' method which, actually, has been pointed out before [3.4.5], but has never been examined. One can notice that slightly different values of the perimeter and average yardstick size are obtained for the same initial yardstick size starting from different contour points (x_s, y_s) . Up to our knowledge, it has never been shown what kind of effects are observed when the calculations are performed starting from different points on the contour. It is not clear what kind of influence this can have on the resulting Richardson plot and fractal dimension. One can expect that the resulting fractal dimension is biased or has a random error within some range for different starting points. In order to analyze the problem a set of measurements was performed using images of artificial fractals shown in Fig. 3.4.1. Such objects have known fractal dimensions and are often used for test purposes.

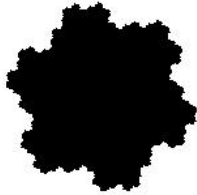
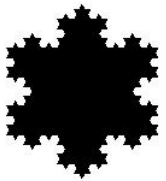
Curve	Image	Known fractal dimension	Number of pixels in the contour	Maximal Feret's diameter
The smoother Koch curve		1.1291	844	149
The triadic Koch curve after third iteration		1.262	1086	144

Fig. 3.4.1. The smoother and triadic Koch curves.

There are two main factors having strong influence on the resulting average yardstick size and the perimeter: the geometry of the figure and the type of digital grid used to acquire the image. First, let us consider the influence of the type of the digital grid. Only the octagonal grid is used in the present study. It is evident that for the minimal possible initial yardstick size equal to 1, the corresponding average yardstick size is always 1 due to the structure of the computer-generated inner 8-boundary on the octagonal grid. For the initial yardstick size equals 2 different nearest approximations of the yardstick length 2 on the octagonal grid can be obtained (Fig. 3.4.2a): 2 and $\sqrt{5}$. Consequently different average values of the initial yardstick size can appear depending on the number of occurrences of the approximations 2 and $\sqrt{5}$ of the initial yardstick size 2. The average yardstick size will be larger than 2 and less than $\sqrt{5}$.

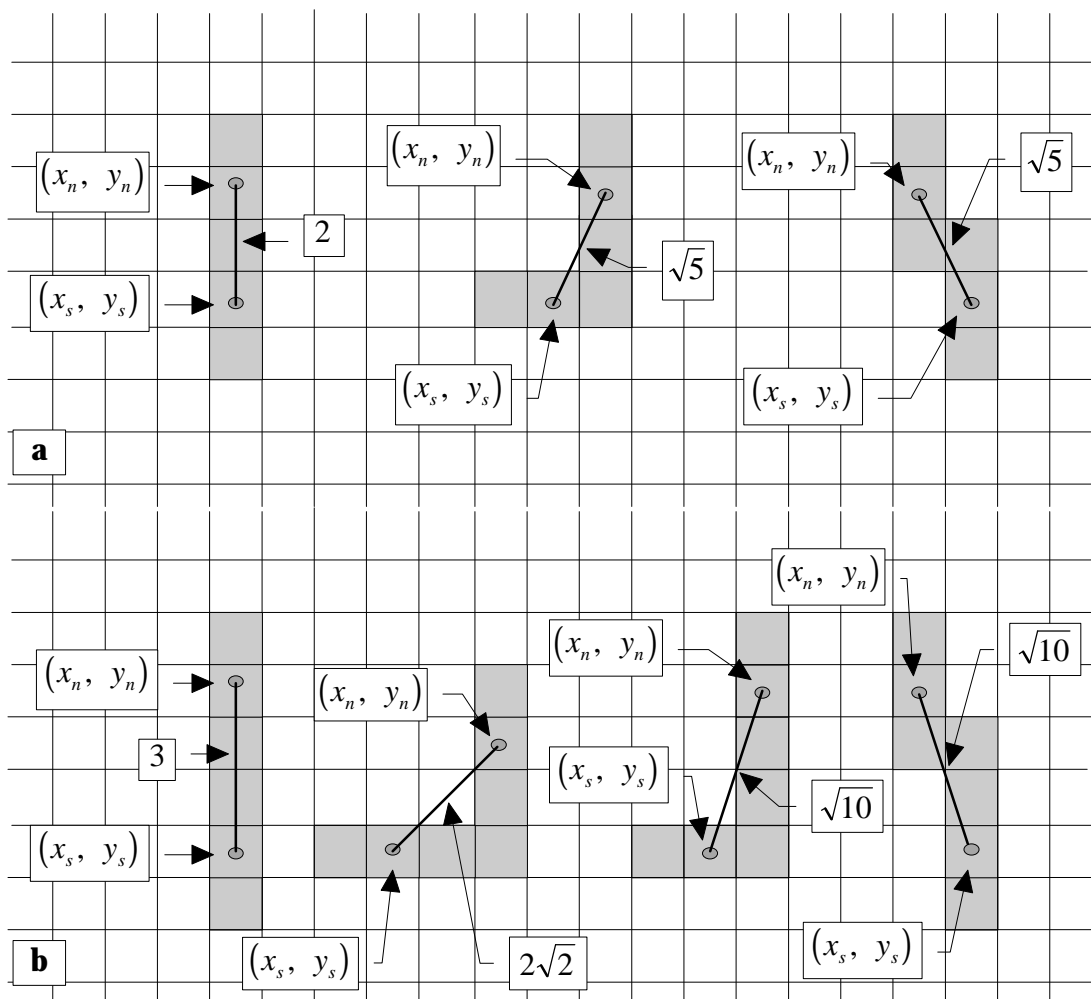


Fig. 3.4.2. Possible approximations of the distances 2 (a) and 3 (b) on an octagonal grid.

The same is expected in the case when the initial yardstick size equals 3, now there are 3 possible best approximations on the octagonal grid: $2\sqrt{2}$, 3 and $\sqrt{10}$ (Fig. 3.4.2b).

In order to show the influence of the geometry of the object on the resulting average yardstick size and the perimeter additional measurements were performed using images of artificial fractals (Fig. 3.4.1) with initial yardstick sizes of 2, 5, 14 and 40. First, the variations of the average value of the yardstick size for different starting points were examined. The graphs of all possible average values obtained for yardstick sizes 2, 5, 14, and 40 for the triadic Koch curve and the smoother Koch curve are shown in Figs 3.4.3 and 3.4.4, respectively. Three facts are evident from these graphs:

- 1) A certain periodicity is observed which is expected because of the iterative nature of the curves resulting in their similarity at different intervals and scales;
- 2) Variations of the average yardstick size increase with increasing initial yardstick size;
- 3) For different objects different variations, even for the same yardstick size, are observed. This is a consequence of the different geometry of the objects.

Probability histograms, obtained for average yardstick sizes 2 and 40, are shown in Fig. 3.4.5. The probability of normally distributed random numbers with the same means and standard deviations as the corresponding average yardstick size distributions for both analyzed objects are shown in the graph as the solid curves. Some statistical parameters describing the distributions are given in Tables 3.4.1 and 3.4.2. The following conclusions can be drawn analyzing these graphs. For small yardstick sizes the geometry of the analyzed object plays a very important role. For example, for the case of the smoother Koch curve the average yardstick size (for initial yardstick size 2) is in the range from 2.127 to 2.132 whereas for the triadic Koch curve it is in the range between 2.114 and 2.117. These intervals are even non-overlapping. Such essential difference can be explained only by the difference in the geometry of the objects. At the same time, for the larger values of the initial yardstick size (for example, 40) the difference in the frequency histograms is not so large. Approximation intervals, obtained for different objects with the same initial yardstick size 40, are almost 80% overlapping. Moreover, experiments show that the frequency histogram better follows the shape of the frequency histogram of normally distributed random numbers with the same mean and standard deviation, as the initial yardstick size increases.

The graphs of all possible values of perimeters obtained for yardstick sizes 2, 5, 14, and 40 for the triadic Koch curve and the smoother Koch curve are shown in Figs 3.4.6 and 3.4.7.

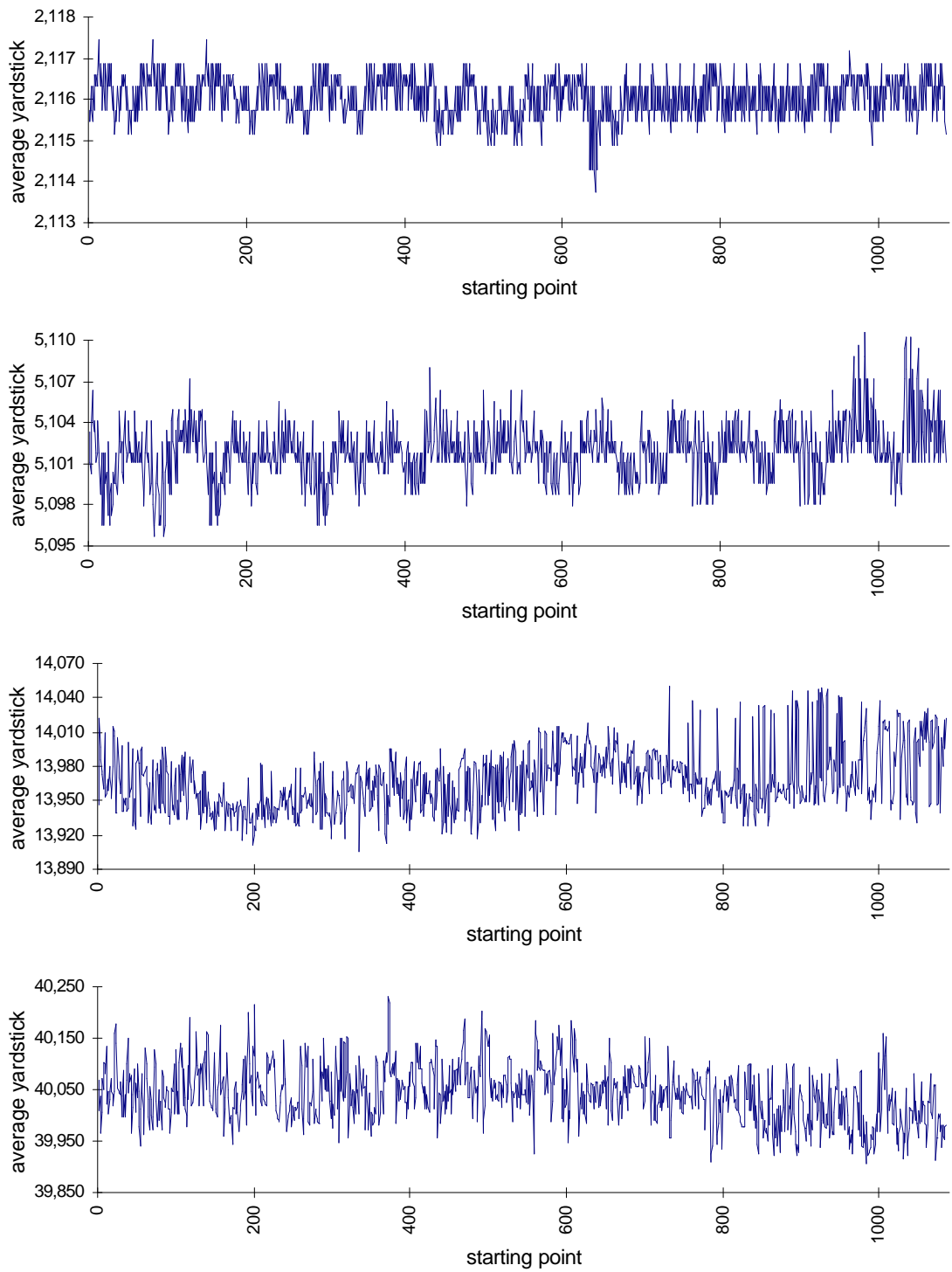


Fig. 3.4.3. All possible average yardstick sizes obtained for initial yardstick sizes of 2, 5, 14 and 40 for the triadic Koch curve.

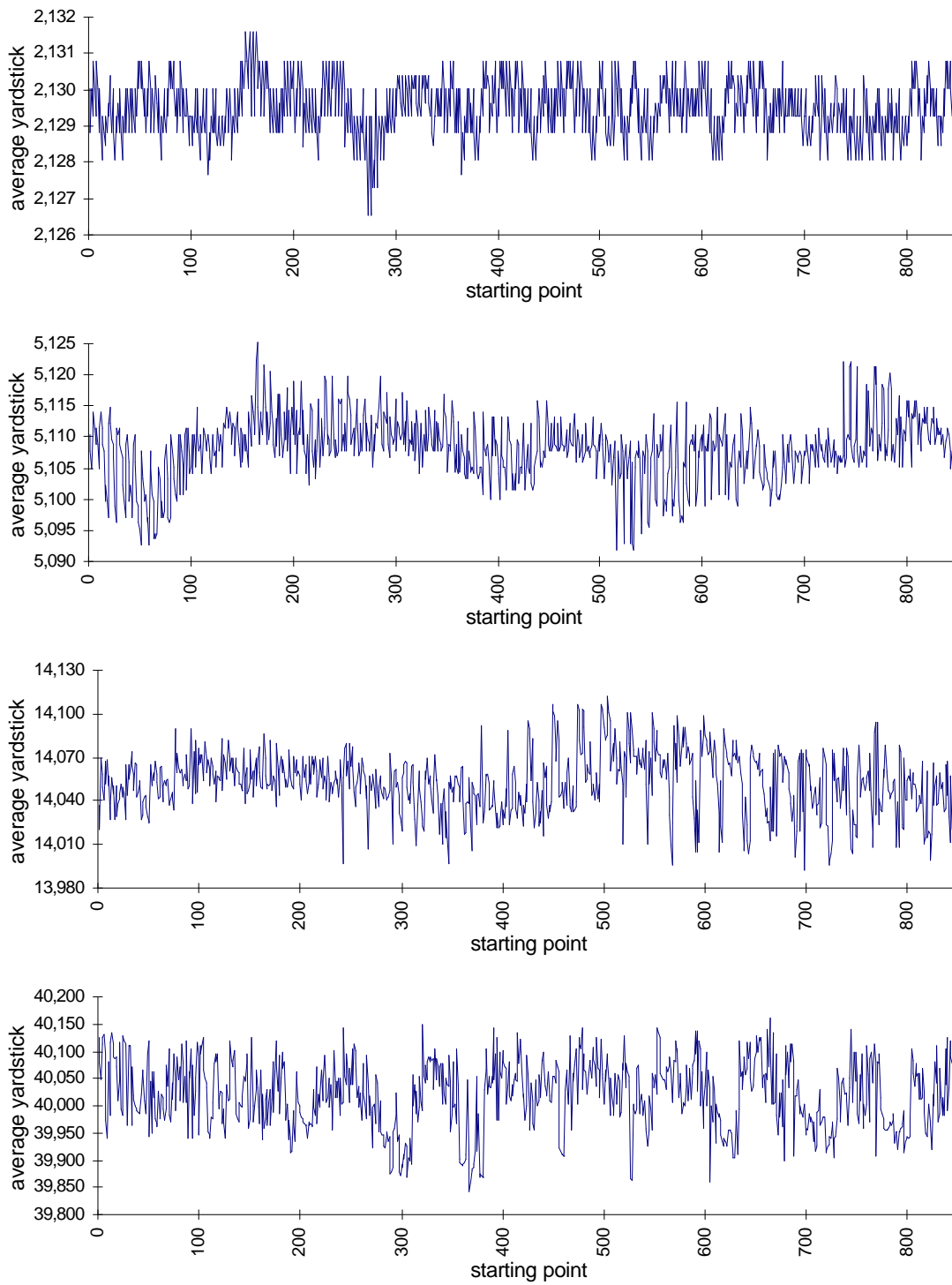


Fig. 3.4.4. All possible average yardstick sizes obtained for initial yardstick sizes of 2, 5, 14 and 40 for the smoother Koch curve.

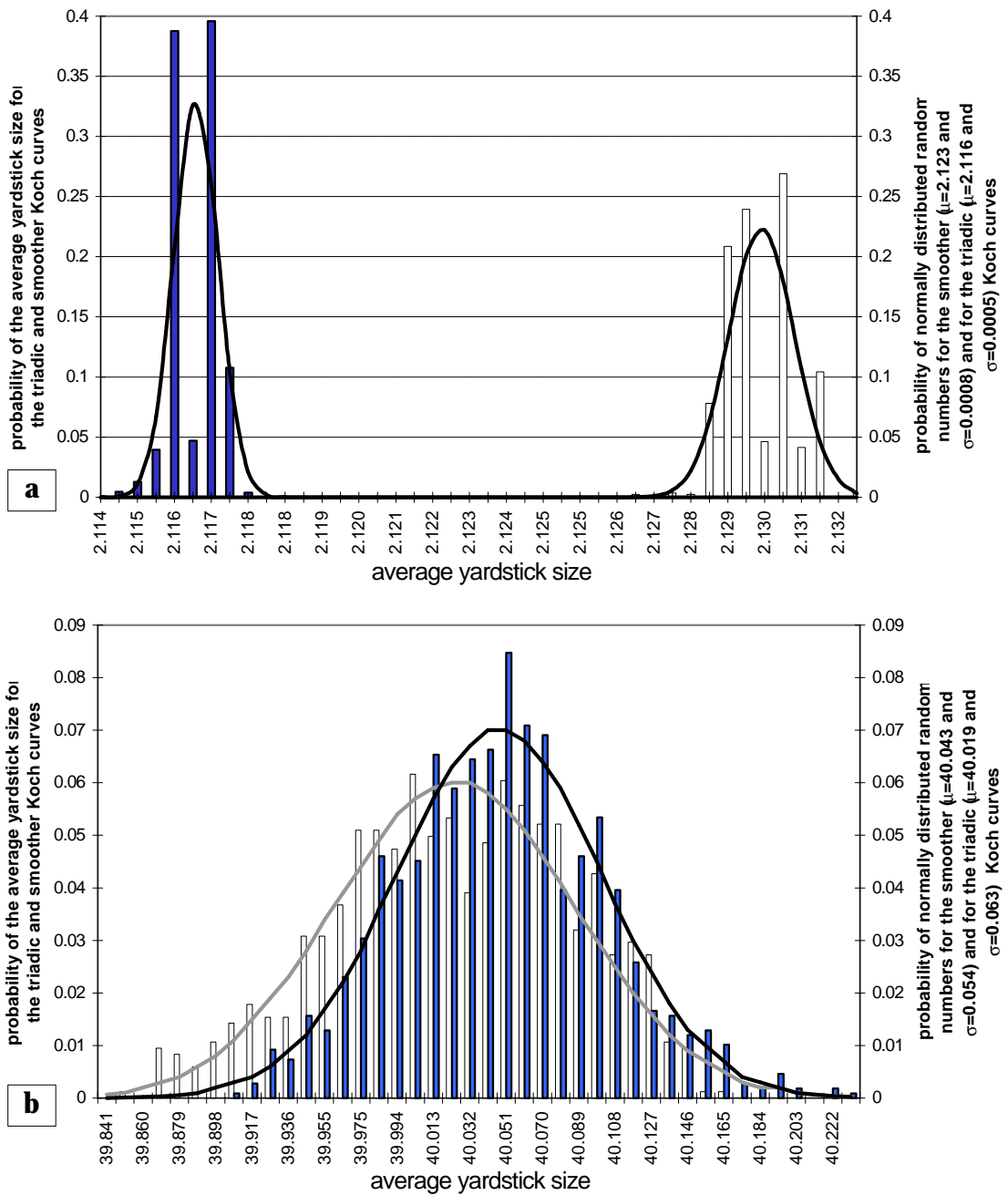


Fig. 3.4.5. Probability histograms for the average yardstick sizes, obtained for the initial yardstick sizes 2 **(a)** and 40 **(b)** for the triadic (black bars) and smoother (white bars) Koch curves. The probability histograms of normally distributed random numbers having the same means and standard deviations as the corresponding average yardstick sizes, are shown as solid lines.

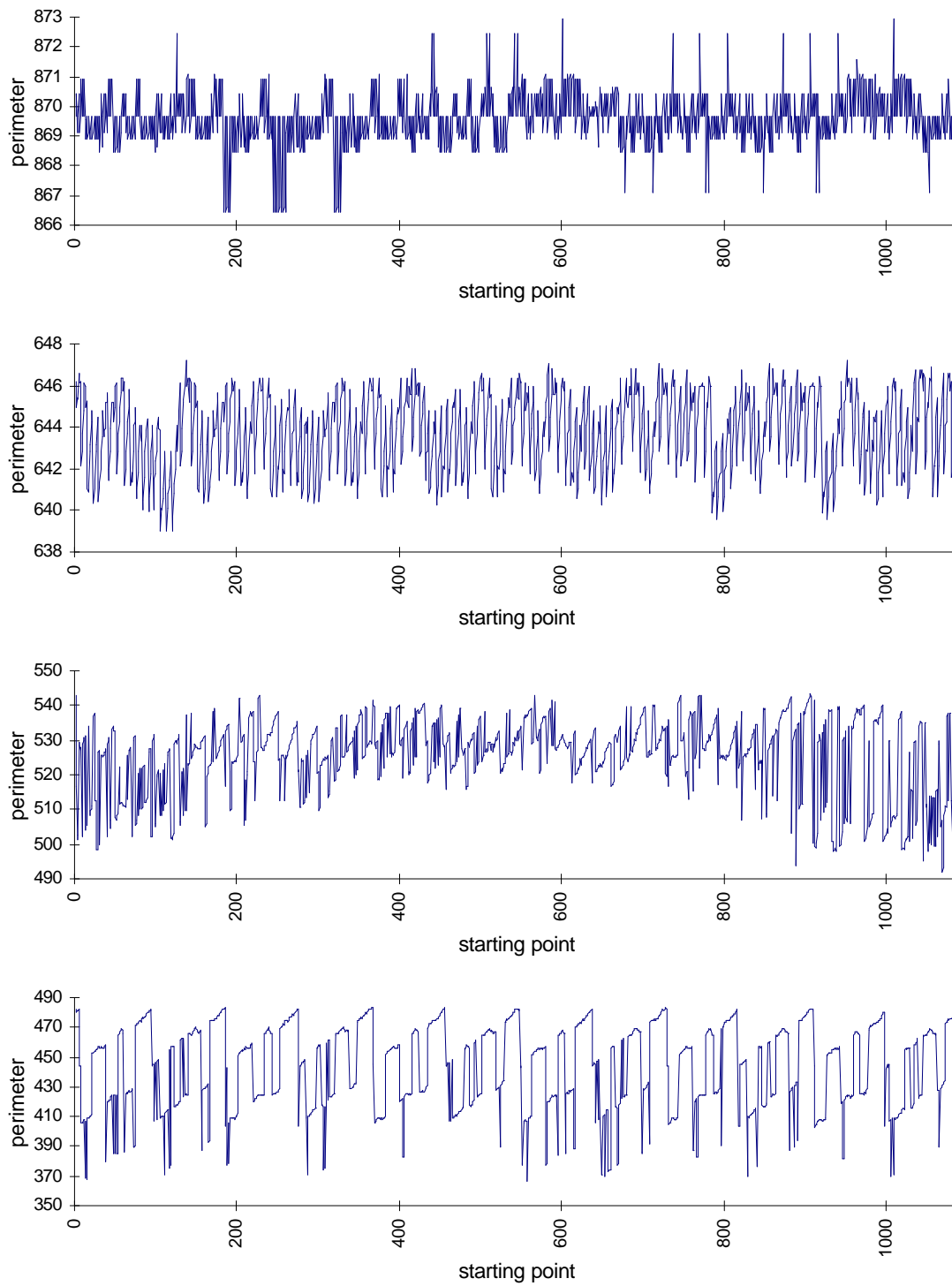


Fig. 3.4.6. All possible perimeters obtained for initial yardstick sizes of 2, 5, 14 and 40 for the triadic Koch curve.

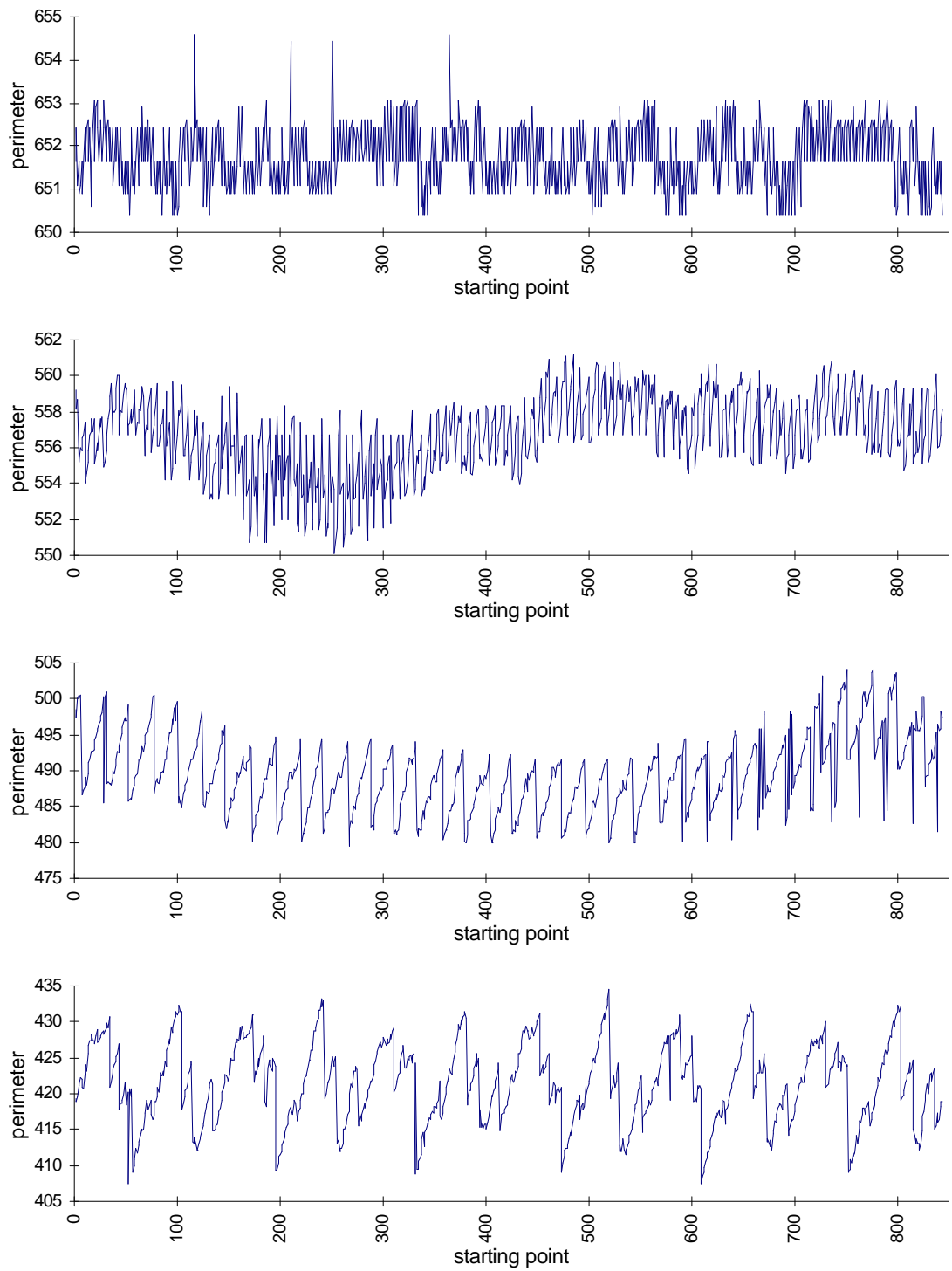


Fig. 3.4.7. All possible perimeters obtained for initial yardstick sizes of 2, 5, 14 and 40 for the smoother Koch curve.

Probability histograms for the perimeter of the triadic and smoother Koch curves approximated with the initial yardstick sizes 5 and 14 are shown in Figs 3.4.8 and 3.4.9. In both cases the shape of the probability distributions is similar to the shape of the probability distributions of random numbers with the same mean and standard deviations. Some statistics about the average yardstick sizes and the perimeters obtained for the initial yardstick sizes 2, 5, 14 and 40 are given in Tables 3.4.1 and 3.4.2.

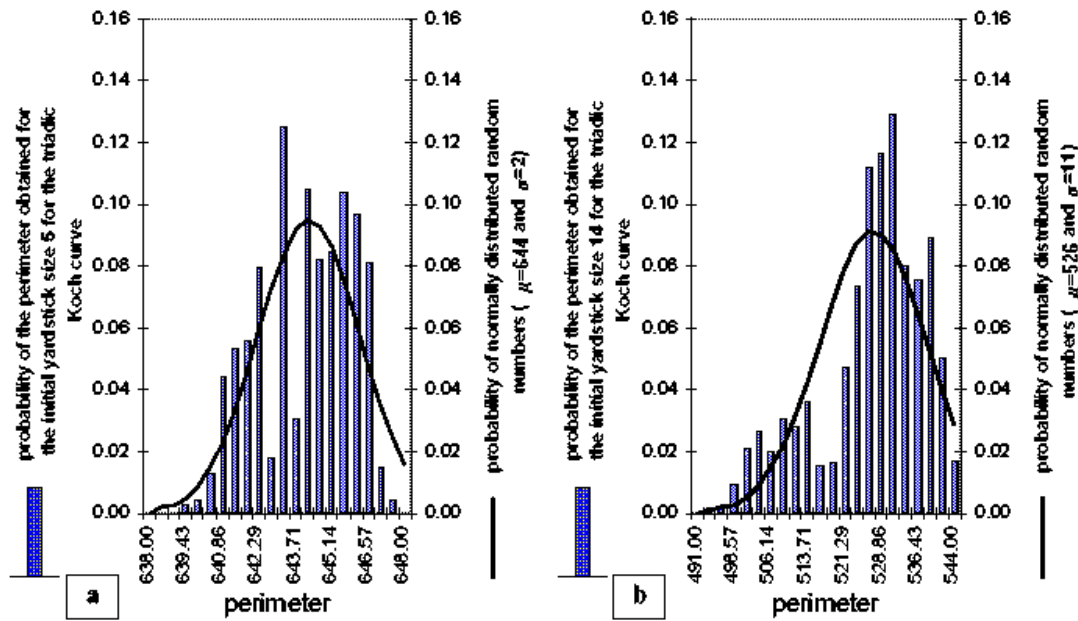


Fig. 3.4.8. Probability histograms for the perimeters, approximated by the initial yardstick sizes 5 (a) and 14 (b) for the triadic Koch curve. The probability histograms of normally distributed random numbers having the same mean and standard deviation are shown as solid lines.

Initial yardstick size	mean of all average yardstick sizes	standard deviation of all average yardstick sizes	average perimeter	standard deviation of the perimeter
2	2.116	0.001	869.58	0.919
5	5.102	0.002	643.78	1.823
14	13.967	0.027	525.53	10.883
40	40.043	0.054	443.45	29.019

Table 3.4.1. Statistics on the average yardstick size and the perimeter for the triadic Koch curve.

Initial yardstick size	mean of all average yardstick sizes	standard deviation of all average yardstick sizes	average perimeter	standard deviation of the perimeter
2	2.130	0.001	651.769	0.711
5	5.108	0.005	556.739	2.127
14	14.053	0.021	489.556	5.148
40	40.019	0.063	421.379	5.476

Table 3.4.2. Statistics on the average yardstick size and the perimeter for the smoother Koch curve.

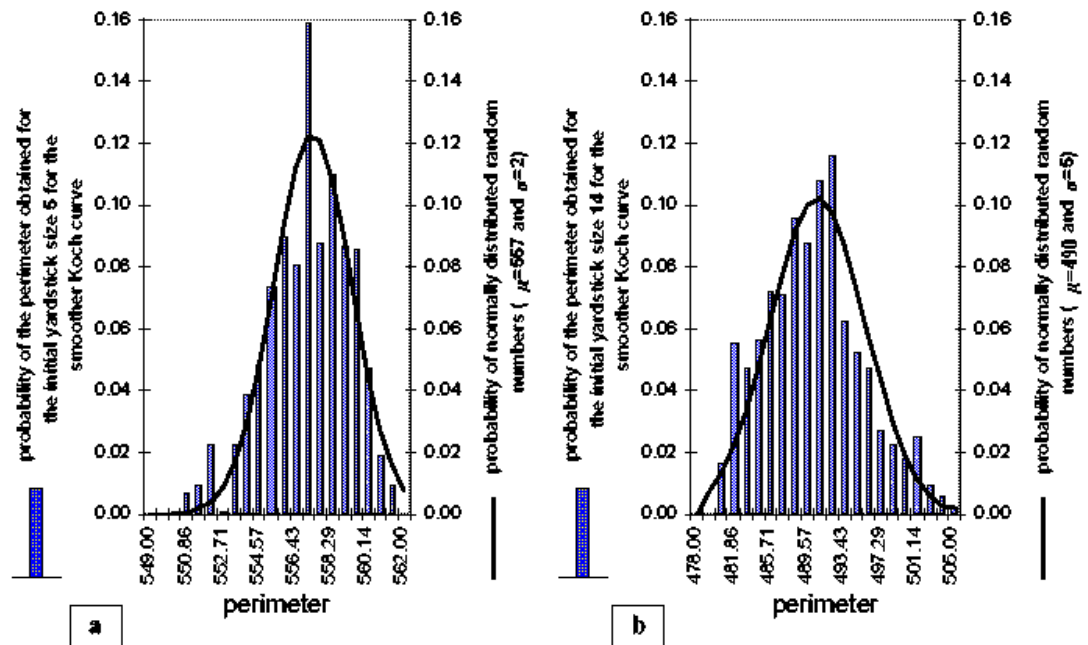


Fig. 3.4.9. Probability histograms for the perimeters, approximated by the initial yardstick sizes 5 (a) and 14 (b) for the smoother Koch curve. The probability histograms of normally distributed random numbers having the same mean and standard deviation are shown as solid line.

It is interesting to examine if there is a correlation between the obtained average yardstick size and perimeter. The coefficients of correlation between different average yardstick sizes and perimeters for different initial yardstick size are shown in Tables 3.4.3 and 3.4.4 for the triadic and smoother Koch curves, respectively. One can observe that there is no correlation between these values.

		average yardstick size obtained for the initial yardstick size (1)				approximated perimeter obtained with the initial yardstick size (2)			
		2	5	14	40	2	5	14	40
(1)	2		-0.163	-0.012	-0.021	-0.169	-0.076	-0.045	-0.061
	5			0.105	-0.075	0.087	0.169	-0.016	0.004
	14				-0.110	0.070	0.071	-0.543	-0.021
	40					-0.020	0.075	0.101	-0.306
(2)	2						0.051	0.031	-0.022
	5							0.122	0.034
	14								0.048
	40								

Table 3.4.3. Coefficients of correlation between the average yardstick sizes and the perimeters obtained for different initial yardstick sizes for the triadic Koch curve.

		Average yardstick size obtained for the initial yardstick size (1)				approximated perimeter obtained with the initial yardstick size (2)			
		2	5	14	40	2	5	14	40
(1)	2		0,017	0,050	0,118	-0,478	-0,015	-0,075	0,066
	5			-0,034	-0,060	0,030	-0,477	0,052	0,050
	14				0,027	-0,054	0,052	-0,317	-0,005
	40					-0,106	0,065	-0,008	0,008
(2)	2						0,013	0,071	-0,009
	5							0,099	-0,084
	14								0,059
	40								

Table 3.4.4. Coefficients of correlation between the average yardstick sizes and the perimeters obtained for different initial yardstick sizes for the smoother Koch curve.

It can be concluded that the average yardstick size as well as the perimeter obtained for a given initial yardstick size have a 'considerable' random error. Experiments show that they

- 1) are different for different initial starting points used to perform the perimeter estimation;
- 2) usually are normally distributed with a mean and standard deviation depending on the geometry of the analyzed object;
- 3) are uncorrelated.

Examples of Richardson plots obtained for the triadic and smoother Koch curves are shown in Fig. 3.4.10.

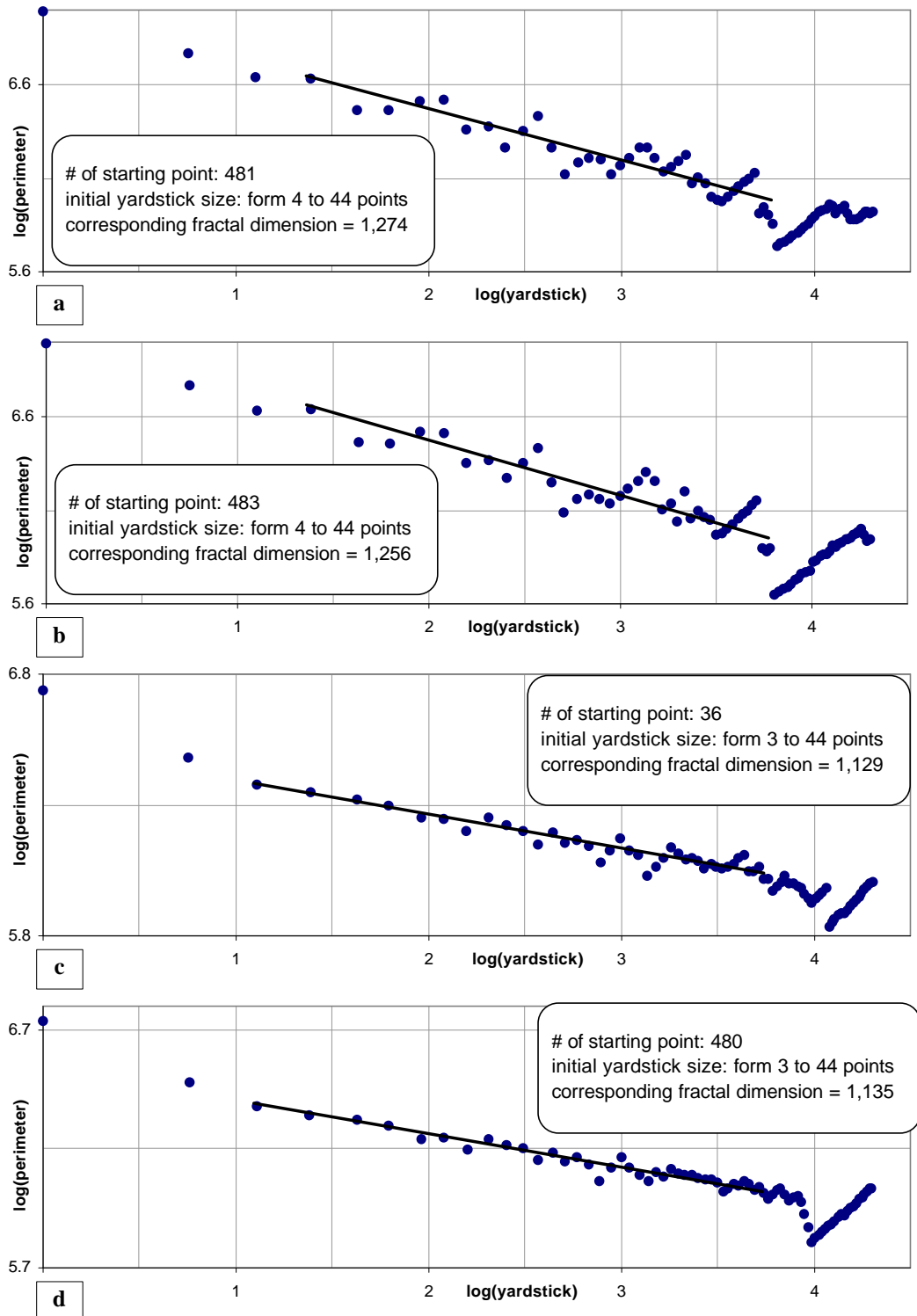


Fig. 3.4.10. Richardson plots obtained for the triadic (a, b) and smoother (c, d) Koch curves using different starting points on the curves.

As seen from these plots, slightly different values of the fractal dimension are obtained when perimeter estimations are performed starting from different starting points. The difference between these values is not significant. However, it is difficult to prove that there are no situations in which this difference is significant. The problem becomes even more complicated when an object having multifractal properties is considered.

3.4.4. Analysis of the Richardson plot

The least-square line fitting in the Richardson plot requires visual inspection of the plot in order to determine the best straight line interval. The following method of an automated analysis of the Richardson plot is proposed. Once the Richardson plot has been constructed we have n points (x_i, y_i) where x_i represents the different yardstick lengths, y_i the values of corresponding estimated perimeters and n the number of data points in the Richardson plot. The statement that there exists a straight line which fits a certain subset of the points implies that there exists a certain inherent structure. The question is then how to reveal this structure. One possible way is to apply a multivariate analysis technique such as cluster analysis (CA), specially intended to solve such types of problems. However, in order to directly apply CA to this specific case, the problem should be reformulated as follows. Let us, instead of all n points in the plot, consider all possible straight lines each of which fits any ordered subset of m points from left to right in the plot ($m = k, k + 1, \dots, n$ where k is certain lower limit). Each of these lines is characterized by its slope a and intercept b . The best fit values of a and b in the least squares sense are calculated as [3.4.1]:

$$a = \frac{m \sum_{i=1}^m x_i y_i - \sum_{i=1}^m x_i \sum_{i=1}^m y_i}{m \sum_{i=1}^m x_i^2 - \left(\sum_{i=1}^m x_i \right)^2} \text{ and } b = \frac{1}{m} \left(\sum_{i=1}^m y_i - a \sum_{i=1}^m x_i \right)$$

From the point of view of determining the fractal dimension only the slope a is of interest. However, the computation of the expected error σ in the slope involves the calculation of the intercepts. The error is calculated as

$$\sigma = \sqrt{\frac{mS}{m \sum_{i=1}^m x_i^2 - \left(\sum_{i=1}^m x_i \right)^2}}$$

where

$$S = \frac{1}{m-1} \left(\sum_{i=1}^m y_i^2 + mb^2 + a^2 \sum_{i=1}^m x_i^2 - 2 \left(b \sum_{i=1}^m y_i - ab \sum_{i=1}^m x_i + a \sum_{i=1}^m x_i y_i \right) \right)$$

For the purpose of this application it is logical to consider only those straight lines which have slopes in the interval -1 and 0 . Furthermore we restrict ourselves to lines with a slope errors σ not exceeding a certain threshold. This results finally in a one-dimensional set containing all possible slopes. The problem of finding the underlying structure through clustering can now be solved via constructing the frequency histogram. The maxima in the histogram show the most populated cluster(s) which correspond to the most appropriate fractal dimension(s).

The method was tested for different artificially generated and real objects. As a first example the triadic Koch island with theoretical fractal dimension $\log 4 / \log 3 = 1.2618\dots$ was used. The Richardson plot was constructed (Fig. 3.4.11b) by the 'hand and dividers' method as explained above. The frequency histogram of all possible slopes (here and in the following examples $k = 4$, $\sigma \leq 0.01$) is shown in Fig. 3.4.11c. The maximum of the histogram is reached at $|a| = 0.27$ which corresponds to the fractal dimension of 1.27 which is in a good agreement with the theoretical value.

The book by Mandelbrot [3.4.3] contains many examples of artificial islands having various fractal dimensions. Some of them were analyzed by the present method and the following results were obtained. For the smoother Koch island (plate 46 from [3.4.3]) having theoretical fractal dimension $\log 3 / \log \sqrt{7} = 1.1291\dots$ the value 1.14 was obtained. A quadric Koch island (plate 49) was constructed with theoretical fractal dimension 1.5 . As the result of analysis by the present method the value of 1.48 was obtained. Finally, a circle (Fig. 3.4.12a), which is known to be a non-fractal object in Euclidean geometry, was also analyzed. The frequency histogram (Fig. 3.4.12c), obtained from corresponding Richardson plot (Fig. 3.4.12b), shows a fractal dimension of 1.01 which actually means the absence of fractality.

An agglomerate (Fig. 3.4.13a) similar to one of the oldest well known objects with multifractal properties, the Medalia's carbonblack profile [3.4.14], was generated and analyzed in order to check the applicability of the method for characterizing complex multifractal objects. The frequency histogram (Fig. 3.4.13c) shows a global maximum, which reveals a fractal dimension of 1.17 . More thorough analysis of the frequency histogram discloses two local maxima, which correspond to fractal dimensions of 1.08 and 1.13 . The visual inspection of the Richardson plot (Fig. 3.4.13b) shows the two distinct lines (as predicted by our method) which correspond to fractal dimensions of 1.08 (textural) and 1.17 (structural). The value of 1.13 is an average of the textural and structural fractals, measured over the interval $\lambda = 0.01$ to $\lambda = 0.20$ (Fig. 3.4.13b). A similar situation was encountered by Flook [3.4.15] and is discussed in Kaye's book [3.4.6] using the Medalia's carbonblack profile as an example. Kaye shows the presence of both textural (1.10) and structural (1.32) fractal dimensions and discusses his early studies [3.4.16] of the carbonblack profile where an overall fractal dimension of 1.18 was obtained as an averaged. The results of our analysis of the original

Medalia's carbonblack profile as it appears in [3.4.14] are quite similar to that of Kaye: structural fractal dimension of 1.32; textural fractal dimension of 1.13 and average fractal dimension of 1.19. The results of the discussion are summarized in Table 3.4.5 together with some other examples.

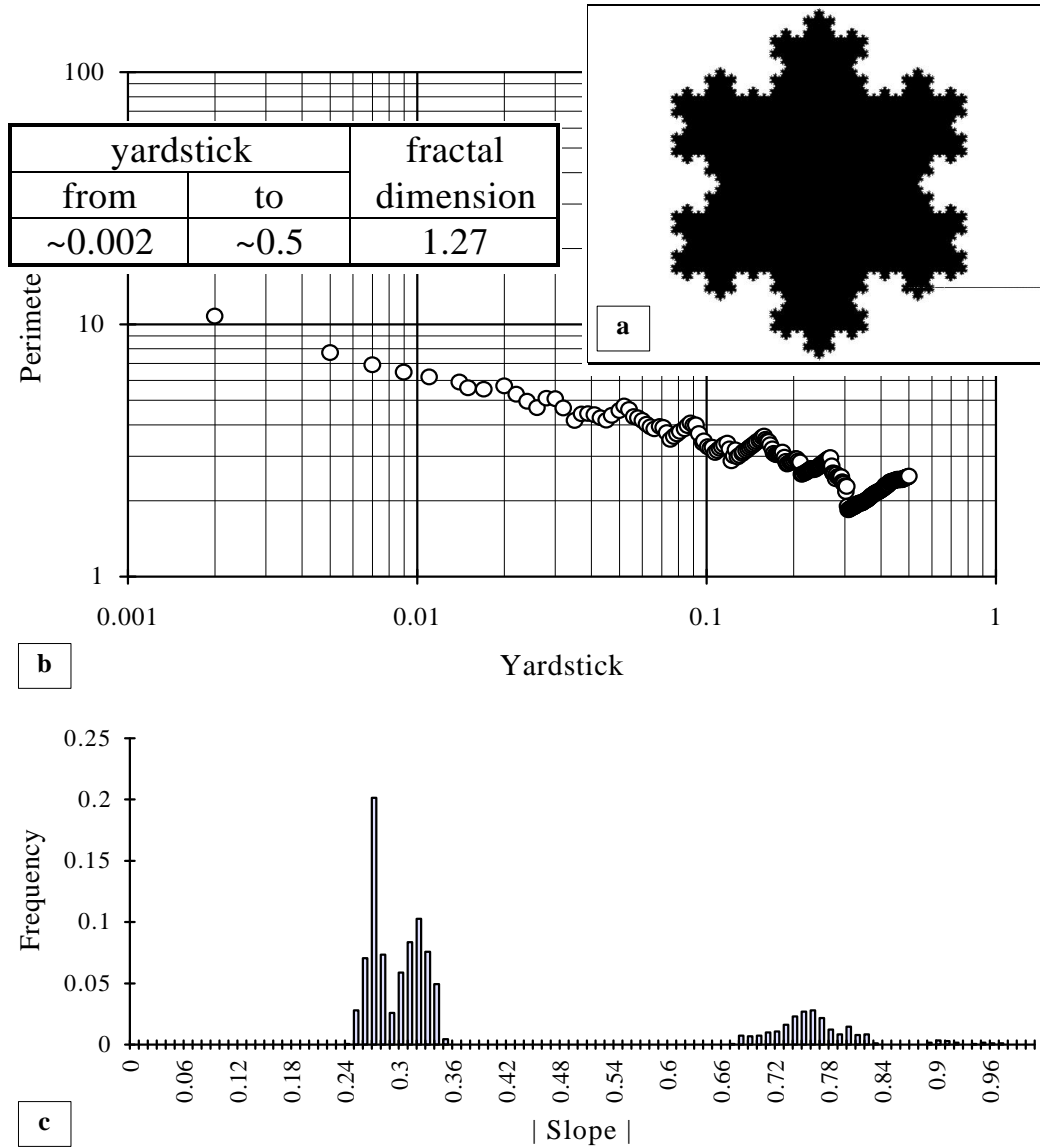


Fig. 3.4.11. a) the triadic Koch island after 5 iterations with theoretical fractal dimension $\log 4 / \log 3 = 1.2618\dots$; b) corresponding Richardson plot (here and in the next figures yardstick and perimeter are shown as fraction of the maximum Feret diameter); c) the frequency histogram, obtained from the Richardson plot shown ($k = 4$, $\sigma \leq 0.01$). Its maximum corresponds to fractal dimension of 1.27.

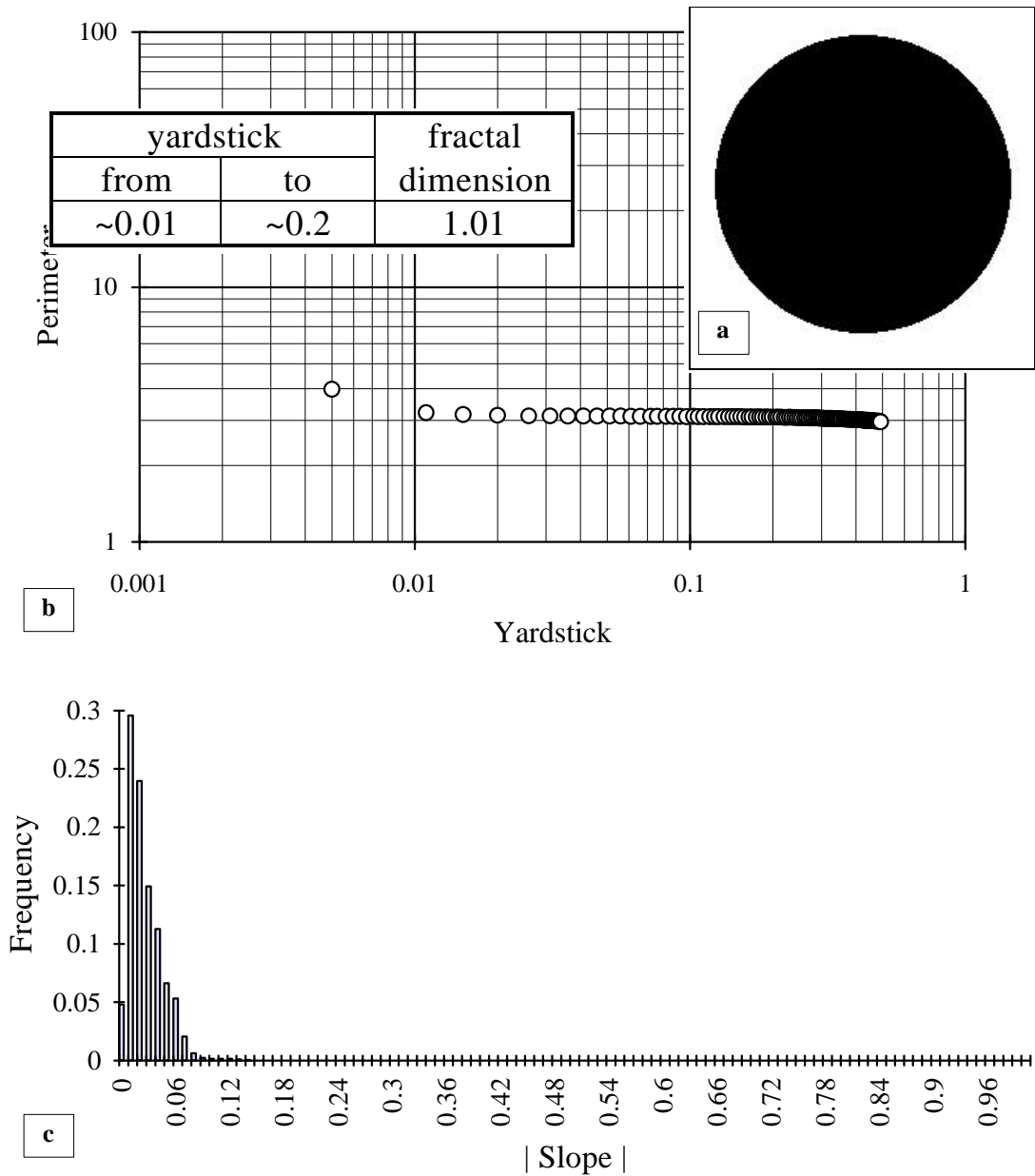


Fig. 3.4.12. **a)** a non-fractal object (a circle); **b)** corresponding Richardson plot; **c)** the frequency histogram, obtained from the Richardson plot shown.

All results shown above have been obtained with $k = 4$ and $\sigma \leq 0.01$. It is interesting to inspect the changes of a frequency histogram vs. k and σ . In order to do this two biological examples were used. Figs 3.4.14a and 3.4.15a show scanning electron microscopy images of individual algae cell and cells agglomerate, respectively. Richardson plots are shown in Figs

3.4.14b and 3.4.15b. One straight line on the plot (Fig. 3.4.14b) can be observed corresponding to a fractal dimension of 1.04. The Richardson plot for the agglomerate of algae cells (Fig. 3.4.15b) shows two straight lines corresponding to textural 1.13 and structural 1.39 fractal dimensions.

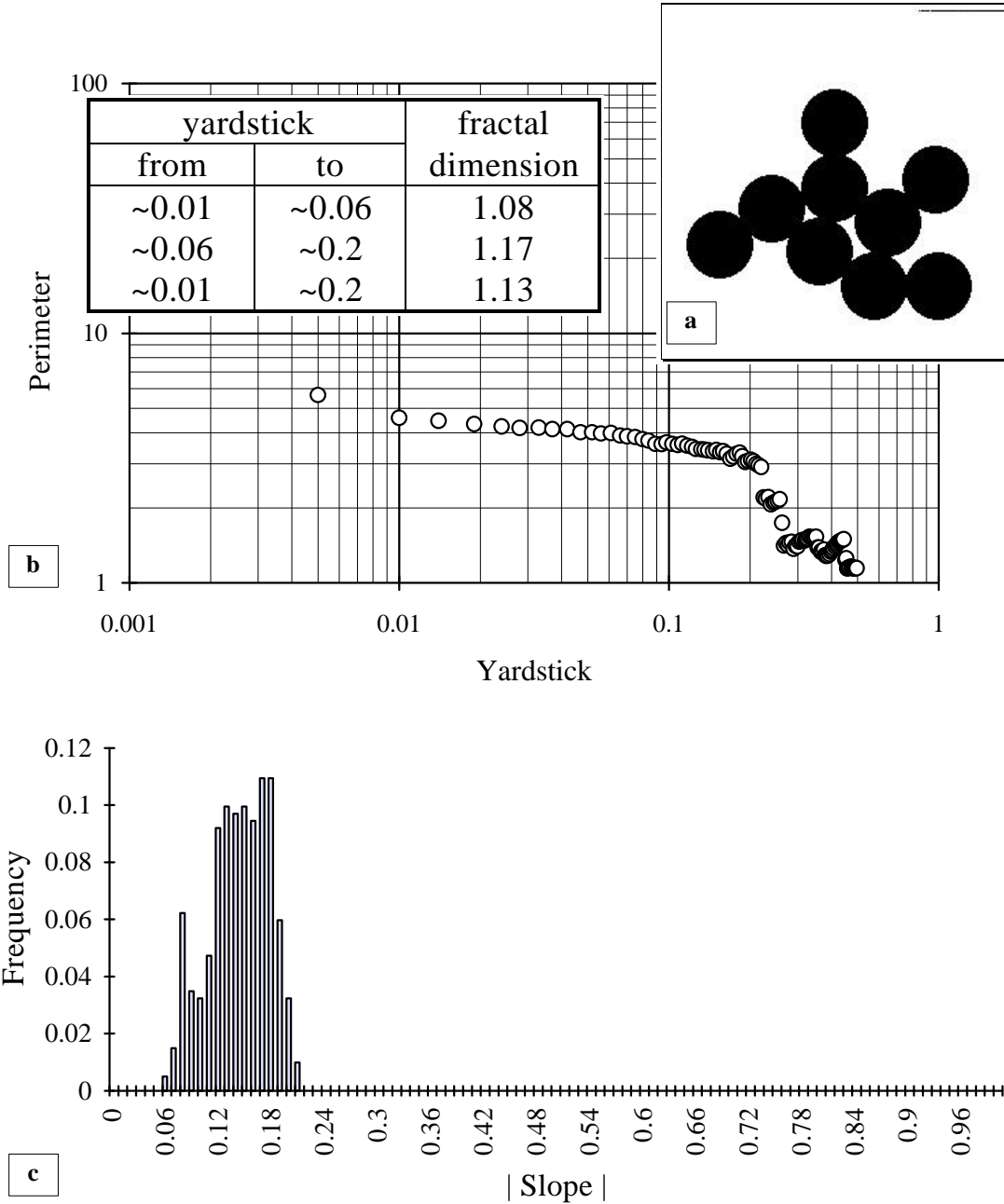


Fig. 3.4.13. **a)** a synthetic agglomerate profile created from the set of circles (similar to the carbonblack profile); **b)** corresponding Richardson plot; **c)** the frequency histogram.

The frequency histograms were obtained for different values of k (Figs 3.4.14c and 3.4.15c) and σ (Figs 3.4.14d and 3.4.15d). Both parameters were chosen in intervals from possibly smallest to reasonably large numerical values. There is no difference in the position of the global maxima for different values of k (Figs 3.4.14c and 3.4.15c). With increasing k some local maxima however can be lost (Fig. 3.4.15c). Thus, numerical value of k should be chosen relatively small in order to obtain a histogram with sufficient detail to reveal the fine structure in the fractal object. Differences of the histograms for different σ are evident especially in case of multifractal object (Fig. 3.4.15d). For relatively small values, the maximum of the histogram corresponds to the textural fractal dimension. Starting from certain larger values the maximum corresponds to the structural one (Fig. 3.4.15d). So, if a relatively small value of σ is chosen the textural fractal dimension can be revealed by the global maximum of a frequency histogram. In the other case, the global maximum corresponds to the structural fractal dimension. Usually there is no essential influence of a chosen value of σ on the location of the maximum of the histogram in the cases when only a single line can be observed on Richardson plot.

Single fractals	Known fractal dimension		Fractal dimension, obtained by the present method	
	textural	structural	textural	structural
circle (Fig. 3.4.12a)	1 (nonfractal)		1.01 ± 0.01	
smoother Koch island [3.4.3]	1.1291...		1.14 ± 0.01	
triadic Koch island (Fig. 3.4.11a)	1.2618...		1.27 ± 0.01	
quadric Koch island [3.4.3]	1.5		1.48 ± 0.01	
coast of Great Britain [3.4.17]	~1.3		1.32 ± 0.01	
algae cell (Fig. 3.4.14a)	-		1.04 ± 0.01	
Multifractals	textural	structural	textural	structural
Medalia's carbonblack profile [3.4.14]	1.10	1.32	1.13 ± 0.01	1.32 ± 0.01
artificially generated carbonblack profile (Fig. 3.4.13a)	-	-	1.08 ± 0.01	1.17 ± 0.01
algae cells agglomerate (Fig. 3.4.15a)	-	-	1.13 ± 0.007	1.39 ± 0.01

Table 3.4.5. Known fractal dimensions and value obtained by the present method for some artificially generated and real objects. Here 'known' means *theoretical* or *from literature*.

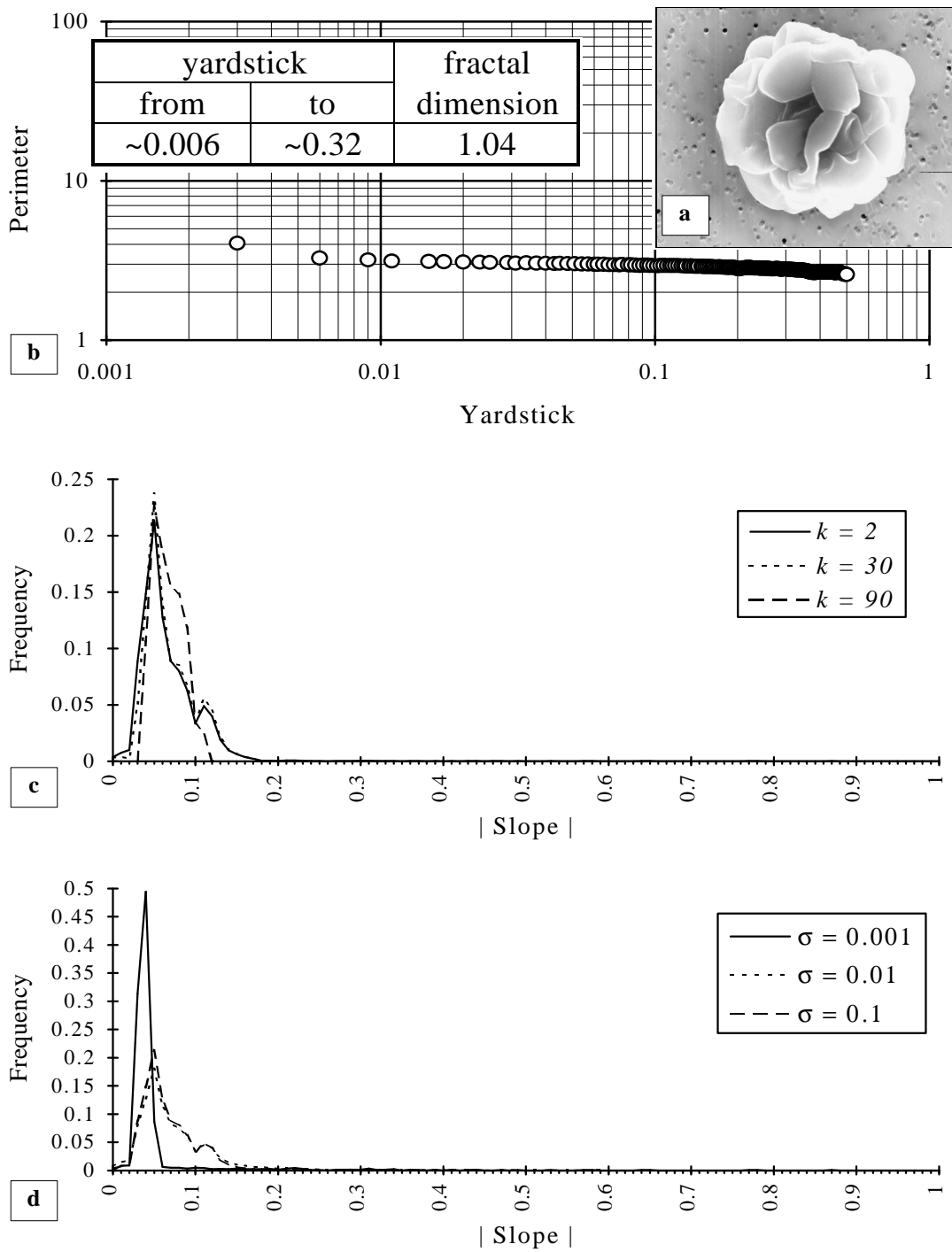


Fig. 3.4.14. **a)** an individual algae cell; **b)** corresponding Richardson plot; **c)** the frequency histogram for parameters $k = 2$, $k = 30$ and $k = 90$ ($\sigma = 0.01$); **d)** the frequency histogram for parameters $\sigma = 0.001$, $\sigma = 0.01$ and $\sigma = 0.1$ ($k = 2$).

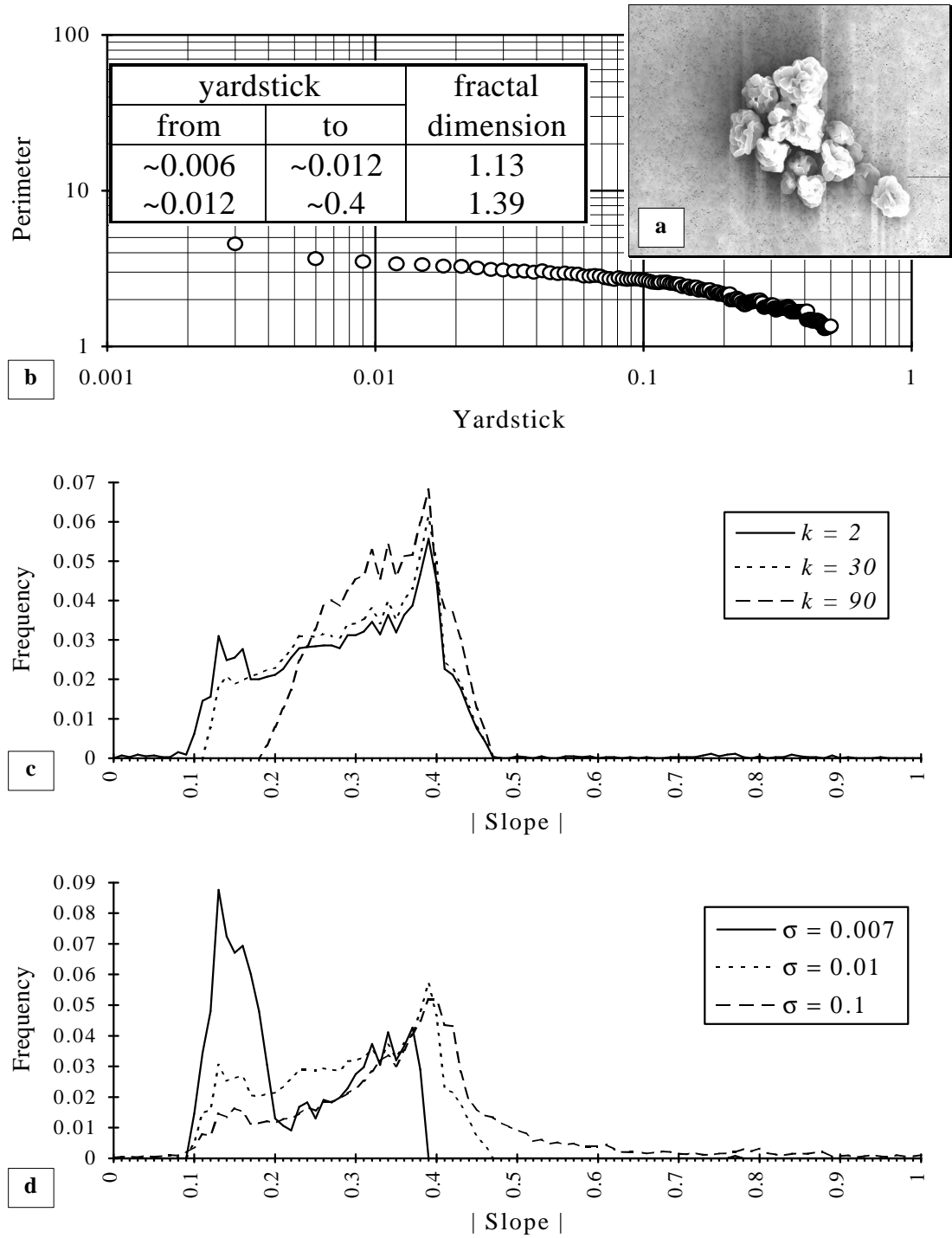


Fig. 4.2.2.15. a) an agglomerate of algae cells; b) corresponding Richardson plot; c) the frequency histogram for parameters $k = 2$, $k = 30$ and $k = 90$ ($\sigma = 0.01$); d) the frequency histogram for parameters $\sigma = 0.007$, $\sigma = 0.01$ and $\sigma = 0.1$ ($k = 8$).

For all studied examples of theoretical and real objects we always found a relation between fractal dimension of an object and a maximum of a corresponding frequency histogram. Depending on the chosen value of σ , a textural or structural fractal dimension can be revealed by the global maximum of the histogram. For a relatively large σ the global maximum corresponds to a structural fractal dimension, whereas for smaller σ it reveals a textural fractal dimension. For single fractal objects the maximum of the histogram doesn't change essentially. In order to reveal the fine structure of the histogram a relatively small value of k should be selected. For most examples discussed above we chose k equal to 4 and σ equal to 0.01 for determining the structural fractal dimension.

3.5. Study of quasi-fractal many-particle systems and percolation networks

Submicron colloidal Ag particles and nano-sized filaments forming a statistical percolation network during '*in situ*' development of double structure tabular microcrystals of AgBr(I) emulsions were studied by zero-loss electron spectroscopic imaging (ZLESI). Image analysis showed that random quasi-fractal clusters are formed in the colloid. ZLESI was applied to characterize the morphology and defect structure of aggregated particles and filaments. To study the cluster structure and its relation to the physical properties, fractal analysis including estimations of cluster fractal dimensions and of density autocorrelation functions was performed. Mechanisms of fractal aggregation based on known models of diffusion limited aggregation, cluster-cluster aggregation and percolation are discussed.

3.5.1. Introduction

Nowadays coagulated fractal and quasi-fractal structures are an area of active research [3.5.1-3.5.2]. They result from a variety of different processes: film deposition on a solid surface, adsorption of molecules by porous matter, solidification of colloids, crystallization of ultradisperse powders, various biophysical processes, etc. As a rule, fractal properties of objects having porous, ramified, rough or sparse and tenuous structures are usually associated with nonequilibrium growth. The unique physical and chemical properties, different from those of both gases and condensed media make fractal clusters of great fundamental interest. Moreover, fractal properties can be used for the characterization of many-particle-systems and microanalysis of surfaces and various disperse substances as well. Volume and surface plasmon excitations, in particular, are determined both by properties of the individual particles and by collective effects due to interaction among the particles densely packed in aggregates. To understand how fractal geometry affects electronic properties of aggregated matter, electron-optical and optical methods can be applied [3.5.3]. Here some data on formation of quasi-fractal clusters in aggregated Ag colloids and of percolation filament networks during development of composite tabular microcrystals of Ag(Br, I) emulsions studied by zero-loss electron spectroscopic imaging (ZLESI) and image analysis are presented.

3.5.2. Experimental

Samples and sample preparation and image acquisition

A suspension of colloidal Ag particles was obtained by reduction of a diluted aqueous solution of AgNO_3 in the presence of 0.1% polyvinyl alcohol (PVA). In another experiments statistical networks of Ag filaments were produced by a 2-minute 'in situ' treatment, with the Kodak D-19 developer, of double structure tabular microcrystals; the latter had a size of 7-10 μm and consisted of AgBr cores and Ag(Br, I) shells containing 5-6 mol. % of AgI. Samples for observations were prepared by deposition of particles and developed crystals on TEM grids covered with a thin carbon film. A ZEISS EM 902 electron microscope with an integrated prism-mirror-prism energy filter operated at 80 kV accelerating voltage was used for ZLESI measurements. The exit energy-selecting slit in the image mode was 10 eV. Digital images of particles were acquired via a SIT TV camera by a KONTRON IBAS 2000 image analysis system.

Image processing and analysis

Quantitative image processing was done to perform fractal analysis of particle aggregates as well as to estimate the parameters of the size distribution of the particles. Selected fields in the latter case contained 500 distinguishable particles.

In order to separate particles from their background, the correlation criterion based technique described in Part 1 has been applied. The crack following algorithm, which is also described in Part 1, has been used for the contour extraction. Estimation of fractal dimensions has been performed using the following techniques:

- 1) the 'hybrid' method (discussed in the previous part) searching the relation $P \sim L^{1-D}$ between the perimeter P of the cluster's projection on an image plane and a 'yardstick' size L used for the measurement of the perimeter;
- 2) the box counting method [3.5.4] based on the relation $N \sim S^{-D}$ between the number of boxes N covering the cluster projection contour on the image plane and their side S ;
- 3) the covering set method [3.5.4] using the relation $N \sim S^{-D}$ between the number of boxes N needed to covered the cluster projection and their side S ;
- 4) the Forrest-Witten technique [3.5.5] based on the relation $N \sim S^D$ between the number of primary particles N within a square of side S plotted on the projection plane of the cluster;
- 5) the density autocorrelation analysis [3.5.5] was done to evaluate the relation $C(r) \sim r^{D-d}$,

between the average density $C(r)$ of occupied points in the projection plane of the cluster at a distance r . Here d is dimension of space ($d = 2$).

Testing of some techniques on a Sierpinsky carpet with the fractal dimension 1.89 gave the following results: 1.80 ± 0.19 (the covering set method); 1.89 ± 0.13 (the Forrest-Witten technique); 1.91 ± 0.11 (the pair correlation function analysis). Analysis of the triadic Koch curve with theoretical fractal dimension 1.26 gives the following results: 1) 1.25 ± 0.07 (the 'hybrid' method); 2) 1.26 ± 0.15 (the box counting method).

3.5.3. Results and discussions

Ag colloids

TEM micrographs of colloidal Ag particles are shown in Fig. 3.5.1. A zero-loss filtered image (Fig. 3.5.1.b) demonstrated a higher contrast and better resolution than the corresponding unfiltered image (Fig. 3.5.1.a) because the blurring and the chromatic aberration caused by inelastically scattered electrons in the specimen is avoided. This allowed to observe more clearly grain boundaries and crystalline defects, e.g. twins and stacking faults.

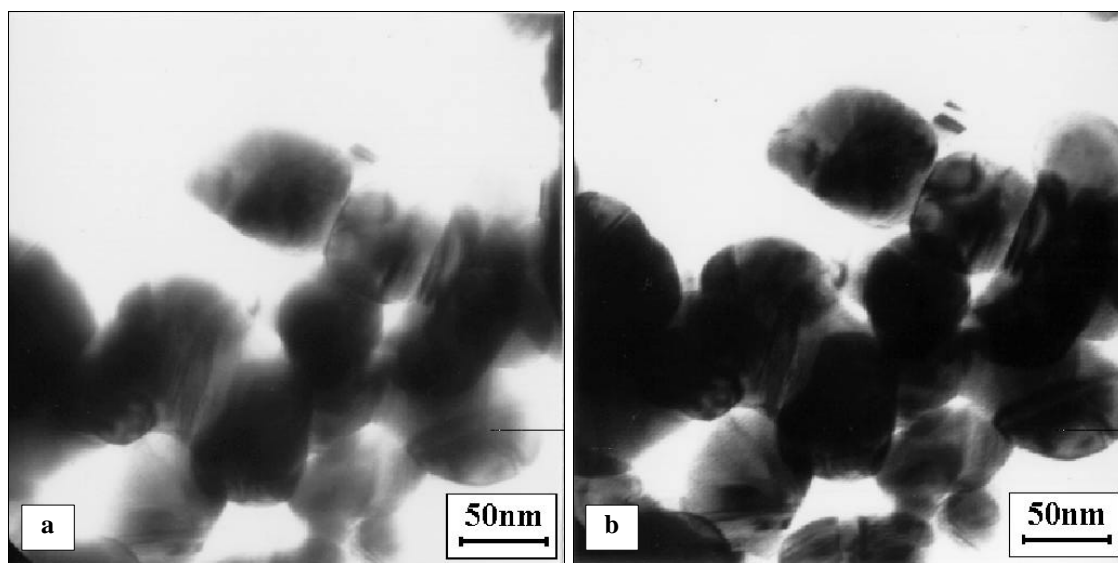


Fig. 3.5.1. TEM images of colloidal Ag particles stabilized with a protective polymer: **a)** CTEM image; **b)** ZLESI image.

Fig. 3.5.2 shows a low magnification view of a cluster formed by colloidal particles. The inset

presents a discrete ring zero-loss spectroscopic selected-area electron diffraction pattern of aggregated particles pointing to a face centered cubic polycrystalline structure. Zero-loss filtering in this case removed the inelastically scattered electrons, which contribute to the background, and increased the contrast of the diffraction patterns. The particle size distribution could satisfactorily be fitted to a log-normal curve with a mean size (equivalent circle diameter) of 42.7 ± 2.2 nm.

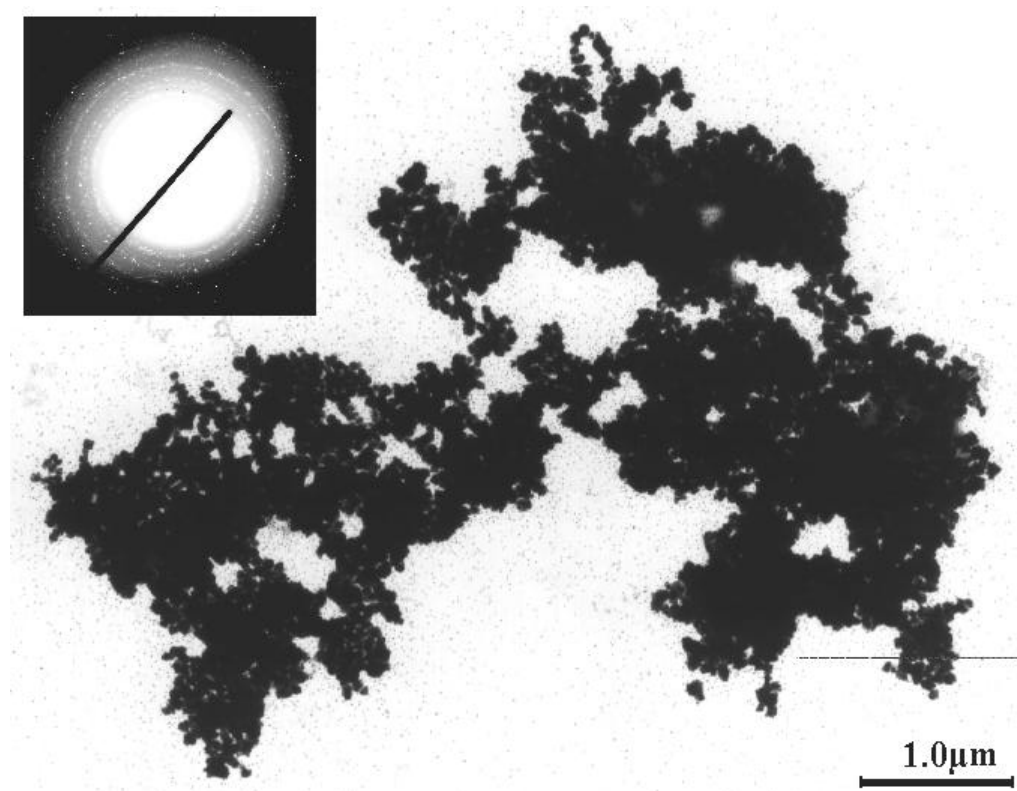


Fig. 3.5.2. ZLESI image of a fractal cluster formed by the particles. Left inset shows a zero-loss spectroscopic selected-area electron diffraction pattern.

Usually the particles in such colloids are prevented from aggregation by repulsive forces between double layers at the particle surfaces. These forces overcome the Van der Waals attraction. Addition of ions to the colloidal system affects the space charge of the particle surfaces and induces aggregation. Initially this leads to coagulation aggregates. Neighborhood particles in the aggregates are separated by thin ion shells at their surface. By aging of the colloidal system the neighborhood particles coalesce partially and build a common grain boundary. The pictures in Fig. 3.5.1 demonstrate the topological arrangement of a statistical network consisting of random aggregates and irregular chains of coagulated particles. The

aggregate shown in Fig. 3.5.2 apparently consists of three parts formed at earlier stages by cluster-particle aggregation. The actual aggregation cannot adequately be described by a model of cluster-particle (CPA) or cluster-cluster (CCA) aggregation only. Real processes may involve these two mechanisms occurring simultaneously or sequentially and/or more complicated aggregation mechanisms. The average density of the aggregate, estimated by the autocorrelation density technique, decreased with increasing radius of gyration in accordance with the CCA model which preferentially contributes to the final stage.

An essential feature of the studied colloids is a power law relationship $M \sim R^{D_\beta}$ between the mass M (or the number of particles) and the radius of gyration R of the aggregate (Fig. 3.5.3). Here D_β is the mass fractal dimension characterizing a given population of aggregates. It is significant that at the early stages of aggregation clusters forming by the CPA mechanism contain a small number (100-300) of specks and therefore cannot be considered as fractals in the strict sense of the word [3.5.6]. In this case the parameter D_β describes the distribution of the substance in the system. However, the high values of the correlation coefficient of linear regression (0.98) indicate that even in this range the fractal approach is appropriate for describing disordered aggregated structures.

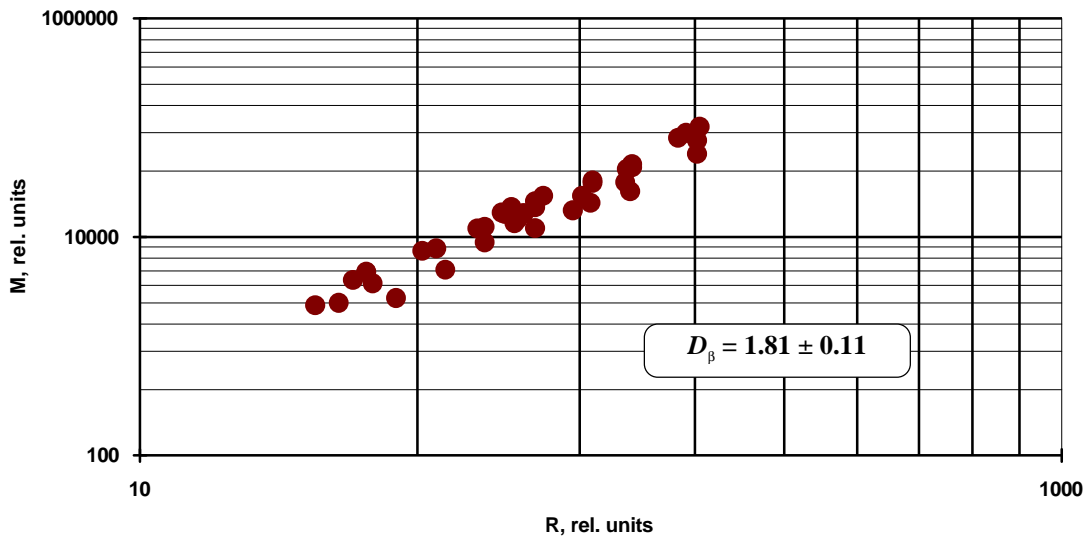


Fig. 3.5.3. Mass dependence of the clusters vs. their size.

Analysis of a population of 39 clusters gave the value $D_\beta = 1.81 \pm 0.11$. This result can be compared with the value 1.81 ± 0.05 obtained for computer simulated diffusion limited aggregation (DLA) growth of fractal clusters along random linear trajectories [3.5.7]. The model developed for describing the 3D cluster aggregation was shown to be in agreement

with results obtained by the Forrest-Witten technique. Since we consider preferentially 2D aggregated structures, the cluster mass determined from the projection will be approximately equivalent to the total mass of the object in three dimensions. Also, the radius of gyration, obtained from the projection, will be essentially the same value determined from the 3D structure. Thus the projection demonstrates the same behavior as the corresponding 3D cluster. This may explain why our data are in good agreement with results for the simulated 3D cluster aggregation. The values of the fractal dimension obtained by the Forest-Witten technique, which characterize the internal automodeling of separate aggregates were in the range 1.86-1.91.

Most of quasi-fractal clusters analyzed by the 'hybrid' method exhibited contour fractal dimension values in the range from 1.20 to 1.35. The values obtained by the box counting methods were 1.30-1.45. This reflects an irregular shape of the outer border cluster structures. The interpretation of these data, which, in principle, can be used for the classification of the structures studied, requires further analysis including also an evaluation of boundary effects.

Ag filament networks

Fig. 3.5.4a shows a ZLESI image of the central part of a double structure tabular microcrystal after a 2-minute *in situ* treatment with the Kodak developer D-19. Development of crystals was usually accompanied with an intensive etching and resulted in the formation of a network of Ag filaments in the core region [3.5.8]. Here again zero-loss filtering allowed to improve the contrast and resolution of filament fine features, i.e. grain boundaries, twins and stacking faults. The development process in the shell regions occurred more slowly and etching was not so intensive because of the lower solubility of $\text{AgBr}_{1-x}\text{I}_x$ as compared to pure AgBr. In the central part of the crystal, Ag filaments and particles formed branched web-like statistical networks. Generation of disordered aggregated structures by silver filaments and particles is obviously related to the stochastic nature of the development process in specific conditions, i.e., the local excess of the active volume developer and the high overpotential of the anode step of the reaction, the occurrence of both direct chemical and solution physical development mechanisms, and the presence of a protective polymer layer on the crystal surfaces [3.5.9]. Moreover, the obtained results suggest that the networks arise in some type of critical process, where such features as self-similarity, scaling and universality are displayed, and which, in principle, may be suitably described by percolation [3.5.10]. The power-law behavior of the silver mass M (the number of occupied sites) vs. the square size S shown in Fig. 3.5.4b points out that the networks belong to random fractals. The fractal dimension determined from the slope of the curve was 1.95 ± 0.11 .

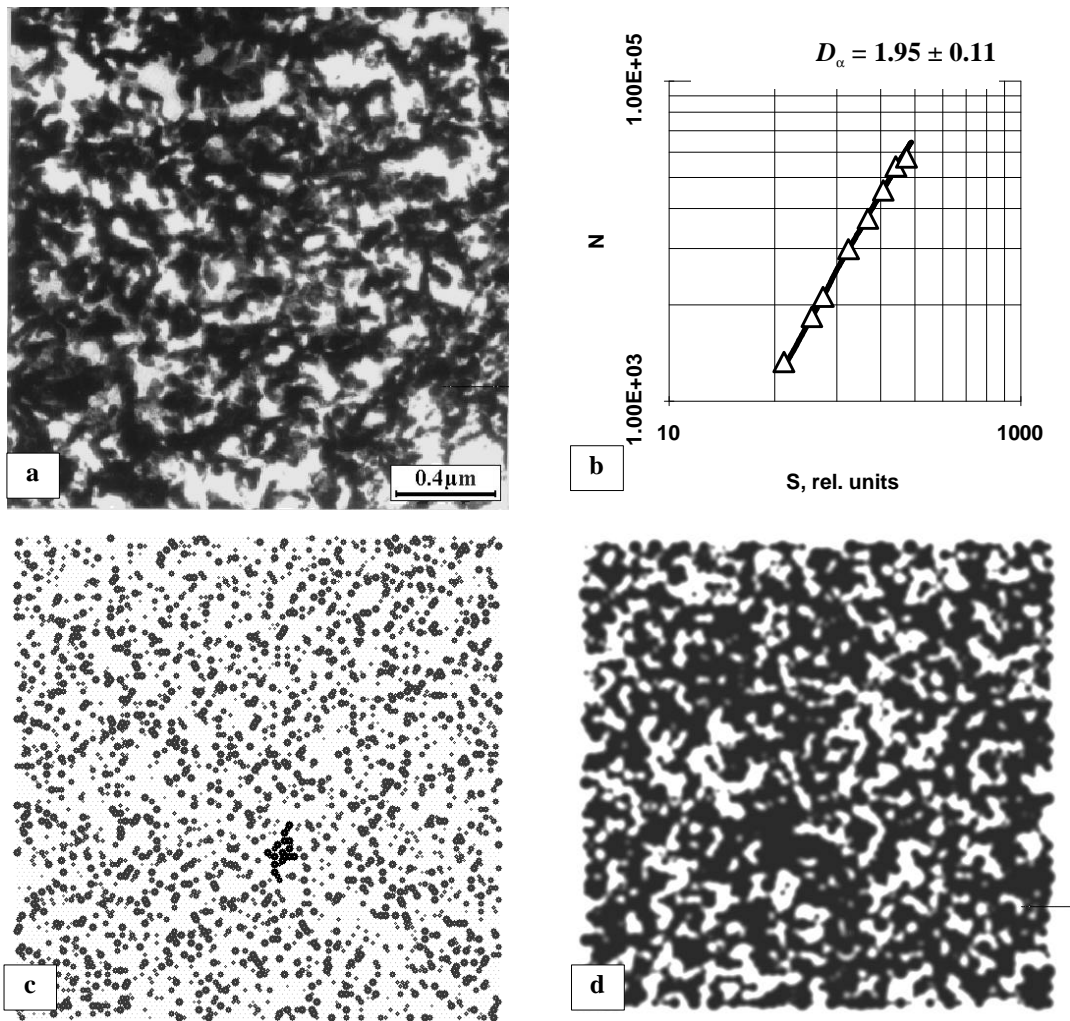


Fig. 3.5.4. a) ZLESI micrograph of a network of Ag filaments formed in the course of a 2-minute development of a double structure AgBr(I) tabular microcrystal; b) the number of occupied sites plotted vs. the square size plotted on the image of the network; c) computer simulation of growth of a percolation network (probability of the occupation of a lattice site $p = 0.2$); d) computer simulation (final stage, formation of the branched network, $p = 0.7$). The line in graph (b) corresponds to the experimental image (a), points obtained by the treatment of the simulated image (d) are shown by triangles.

Numerical computations of the network growth within a simplified invasion percolation model [3.5.11] shown in Figs 3.5.4c and 3.5.4d describe, respectively, an initial stage and a final stage of the aggregation process with a hexagonal lattice. At the final stage a simulated extended network obviously exhibits the morphology of filaments similar to that on the ZLESI image in Fig. 3.5.4a.

The value of fractal dimension for the simulated network shown in Fig. 3.5.4d is 1.94 ± 0.11 in satisfactory agreement with the experimental value (Fig. 3.5.4b). It was also found that in both cases the autocorrelation function $C(r)$ demonstrates a similar behavior. Based on the obtained results, one can conclude that this model can be applied to describe the filament network growth in the course of the photographic development process.

3.5.4. Conclusions

This study shows that ZLESI and digital image analysis are useful for the characterization of coagulated Ag colloids and of chemically generated statistical networks of Ag filaments formed during '*in situ*' development of composite Ag(Br, I) tabular microcrystals. The data presented point out that aggregated Ag particles of 42.7 ± 2.2 nm in size deposited onto an inert carbon support form random quasi-fractal clusters. The mass fractal dimension of the clusters was estimated as 1.81 ± 0.11 in line with data on simulation of the fractal cluster growth according to the DLA model. Box fractal dimension of a random network of nano-sized Ag filaments formed in the course of development of double structure tabular microcrystals of Ag(Br, I) emulsions was determined as 1.95 ± 0.11 in satisfactory agreement with numerical computations of the network growth within the invasion percolation model.

References

- [3.1.1] R. Duda and P. Hart, *Pattern Classification and Scene Analysis*, Wiley, New York, 1973.
- [3.1.2] N. Clark, *Three techniques for implementing digital fractal analysis of particle shape*, Powder Technology, vol. 46, pp. 45-52, 1986.
- [3.1.3] M. Normand and M. Peleg, *Determination of the fractal dimension of a particle silhouette using image-processing techniques*, Powder Technology, vol. 45, pp. 271-275, 1986.
- [3.1.4] P. Hopke, G. Casuccio, W. Mershon and R. Lee, *The use of fractal dimension to characterize individual airborne particles*, Scientific Computing and Automation (Europe), pp. 173-178, Elsevier, Amsterdam, 1990.
- [3.1.5] S. Cheng, J. Lin, J-R. Wu and J. Gentry, *Test cases for examination of fractal dimension*, Journal of Aerosol Science, vol. 25, suppl. 1, pp. S379-S380, 1994.
- [3.1.6] B. Kaye, *A Random Walk Through Fractal Dimensions*, VCH, Weinheim, 1989.
- [3.1.7] J. Fisher, B. Prentice, D. Silberman, J. Ondov, A. Biermann, R. Ragaini and A. McFarland, *Physical and morphological studies of size-classified coal fly ash*, Environmental Science and Technology, vol. 12, pp. 447-451, 1978.
- [3.1.8] A. Ramsden and M. Shiraoka, *Characterization and analysis of individual fly-ash particles from coal-field power stations by a combination of optical microscopy, electron microscopy and quantitative electron microprobe analysis*, Atmospheric Environment, vol. 16, pp. 2191-2206, 1982.
- [3.1.9] B. Mandelbrot, *The Fractal Geometry of Nature*, Freeman, New York, 1983.
- [3.1.10] J. Orford and W. Whalley, *The use of the fractal dimension to quantify the morphology of irregular-shaped particles*, Sedimentology, vol. 30, pp. 655-668, 1983.
- [3.2.1] T. Wallace and P. Wintz, *An efficient three-dimensional aircraft recognition algorithm using normalized Fourier descriptors*, Computer Graphics and Image Processing, vol. 13, pp. 99-126, 1980.
- [3.2.2] M. Mellou, J. Militky and M. Forina, *Chemometrics for Analytical Chemistry*, vol. 1, 2nd edition, Ellis Horwood Limited, New York, 1992.
- [3.2.3] I. Bondarenko, B. Treiger, P. Van Espen and R. Van Grieken, *IDAS, a Windows-based software package for cluster analysis*, Spectrochimica Acta Part B, vol. 51, pp. 441-456, 1996.
- [3.2.4] J. Zurada, *Introduction to Artificial Neural Systems*, West Publishing Company, New York, 1992.
- [3.2.5] NCS Company, Totton, UK, URL: <http://www.demon.co.uk/skylake>.
- [3.2.6] P. DeNee, *Collecting handling and mounting of particles for SEM*, Scanning Electron Microscopy, vol. I, pp. 479-484, 1978.
- [3.3.1] I. Geuens, *Development of Micro and Surface Analysis Methods for the Quantitative Characterization of Silver Halide Microcrystals*, Ph.D. Dissertation, University of Antwerp, 1993.
- [3.3.2] B. Nys, *The Development of Image Processing and Analysis Techniques for Applications in Chemistry and Biomedicine*, Ph.D. Dissertation, University of Antwerp, 1991.
- [3.3.3] E. Dougherty, J. Mc Cabe, E. Thurston and J. Laskin, *Automated classification of silver halide crystals*, Imaging Science and Technology, pp. 47-50, 1990.

- [3.3.4] B. Raeymaekers, P. Van Espen and F. Adams, *The morphological characterization of particles by automated scanning electron microscopy*, *Microchimica Acta*, vol. 2, pp. 437-454, 1984.
- [3.3.5] J. Matas, Z. Shao and J. Kittler, *Estimation of curvature and tangent direction by median filtered differencing*, *Lecture Notes in Computer Science*, vol. 974, pp. 83-88, 1995.
- [3.3.6] J. Keller, M. Gray and J. Givens, Jr., *A fuzzy K-nearest neighbor algorithm*, *IEEE Transactions on Systems, Man and Cybernetics*, vol. SMC-15, no. 4, pp. 580-585, 1985.
- [3.4.1] J. Russ, *Fractal Surfaces*, Plenum Press, New York, 1994.
- [3.4.2] B. Mandelbrot, *How long is the coast of Britain? Statistical self-similarity and fractional dimension*, *Science*, vol. 155, pp. 636-638, 1967.
- [3.4.3] B. Mandelbrot, *Fractals: Form, Chance and Dimension*, Freeman, San Francisco, 1977.
- [3.4.4] N. Clark, *Three techniques for implementing digital fractal analysis of particle shape*, *Powder Technology*, vol. 46, pp. 45-52, 1986.
- [3.4.5] J. Orford and W. Whalley, *The use of the fractal dimension to quantify the morphology of irregular-shaped particles*, *Sedimentology*, vol. 30, pp. 655-668, 1983.
- [3.4.6] B. Kaye, *A Random Walk Through Fractal Dimensions*, VCH Verlagsgesellschaft, Weinheim, 1986.
- [3.4.7] H. Schwarz and E. Exner, *The implementation of the concept of fractal dimension on semi-automatic image analyzer*, *Powder Technology*, vol. 27, pp. 207-213, 1980.
- [3.4.8] T. Cleary, R. Samson and W. Gentry, *Methodology for fractal analysis of combustion aerosols and particle clusters*, *Aerosol Science and Technology*, vol. 12, pp. 518-525, 1990.
- [3.4.9] Y. Xie, P. Hopke, G. Casuccio and B. Henderson, *Use of multiple fractal dimensions to quantify airborne particle shape*, *Aerosol Science and Technology*, vol. 20, pp. 161-168, 1994.
- [3.4.10] J. Carr and W. Benzer, *On the practice of estimating fractal dimension*, *Mathematical Geology*, vol. 23, no. 7, pp. 945-958, 1991.
- [3.4.11] T. Nonnenmacher, G. Baumann, A. Barth and G. Losa, *Digital image analysis of self-similar cell profiles*, *International Journal of Bio-Medical Computing*, vol. 37, pp. 131-138, 1994.
- [3.4.12] B. Kaye and G. Clark, *Fractal description of extra terrestrial fineparticles*, *Particle Characterization*, vol. 2, pp. 143-148, 1985.
- [3.4.13] D. Stoyan and H. Stoyan, *Fractals, Random Shapes and Point Fields (Methods of Geometrical Statistics)*, John Wiley & Sons, Chichester, 1995.
- [3.4.14] A. Medalia and G. Hornik, *Pattern recognition problems in the study of carbonblack*, *Pattern Recognition*, vol. 4, pp. 155-158, 1975.
- [3.4.15] A. Flook, *The use of dilation logic on the Quantimet to achieve fractal dimension characterization of texture and structured profiles*, *Powder Technology*, vol. 21, pp. 295-298, 1978.
- [3.4.16] B. Kaye, *Specification of the ruggedness and/or texture of a fineparticle profile by its fractal dimension*, *Powder Technology*, vol. 21, pp. 1-16, 1978.
- [3.4.17] J. Feder, *Fractals*, Plenum Press, New York, 1988.
- [3.5.1] J. Chevalier, C. Colliex and M. Tence, *Annular dark-field imaging in a STEM: application to the calculation of the fractal dimension of aggregates of iron particles*, *Journal de*

- Microscopie et de Spectroscopie Electronique, vol. 10, pp. 417-424, 1985.
- [3.5.2] M. Tence, J. Chevalier and R. Julien, *On the measurement of the fractal dimension of aggregated particles by electron microscopy: experimental method, corrections and comparison with numerical models*, Journal de Physique, vol. 47, pp. 1989-1998, 1989, 1986.
- [3.5.3] H. Seiler, U. Haas, B. Ocker and K. Kortje, *Small metallic particles studied by optical and electron-optical spectroscopy*, Faraday Discussions, vol. 92, pp. 121-128, 1991.
- [3.5.4] T. Cleary, R. Samson and J. Gentry, *Methodology for fractal analysis of combustion aerosols and particle clusters*, Aerosol Science and Technology, vol. 12, pp. 518-525, 1990.
- [3.5.5] S. Forrest and T. Witten, *Long-range correlations in smoke-particle aggregates*, Journal of Physics: A: Mathematical and General, vol. 12, no. 5, pp. L109-L117, 1979.
- [3.5.6] V. Oleshko, M. Alfimov, X. Cui and S. Wang, *Study of sulphur sensitization products on the surface of tabular grains of silver halide emulsions by means of analytical electron microscopy and image analysis*, The Journal of Photographic Science, vol. 42, pp. 110-116, 1994.
- [3.5.7] P. Meakin, *Diffusion-limited aggregation in three dimensions: results from a new cluster-cluster aggregation model*, Journal of Colloid and Interface Science, vol. 102, no. 2, pp. 491-512, 1984.
- [3.5.8] V. Oleshko, R. Gijbels, W. Jacob, F. Lakiere, A. Van Daele, E. Silaev and L. Kaplun, *Characterization of double structure tabular microcrystals of silver halide emulsions by means of electron energy-loss spectroscopy, zero-loss electron spectroscopic imaging and energy-dispersive X-ray microanalysis*, Microscopy, Microanalysis, Microstructures, vol. 6, pp. 79-88, 1995.
- [3.5.9] V. Oleshko and M. Alfimov, *Electron microscopic investigation of selective and non-selective reduction of silver halide emulsions*, Journal of Imaging Science and Technology, vol. 38, pp. 162-171, 1994.
- [3.5.10] T. Nakayama, K. Yakudo and L. Orbach, *Dynamical properties of fractal networks: scaling, numerical simulations, and physical realizations*, Reviews of Modern Physics, vol. 66, no. 2, pp. 381-443, 1994.
- [3.5.11] D. Wilkinson and M. Barsony, *Monte Carlo study of invasion percolation clusters in two and three dimensions*, Journal of Physics: A: Mathematical and General, vol. 17, pp. L129-L135, 1984.